

A multifaceted isoneutral eddy transport diagnostic framework and its application in the Southern Ocean

Jingwei Xie¹, Hailong Liu¹, and Pengfei Lin¹

¹Institute of Atmospheric Physics, Chinese Academy of Sciences

November 24, 2022

Abstract

We propose a multifaceted isoneutral eddy transport diagnostic framework that combines the stationary-transient and Leonard's decomposition in large eddy simulation (LES). We diagnose the subfilter flux, the isotropic transport coefficient, and the anisotropic transport tensor or eigenvalues in the Southern Ocean (SO). The anisotropic tensor greatly reduces the reconstruction error of the subfilter flux because of its ability to distinguish the directionality of dynamic information, especially the topographic effect. A thorough analysis of the anisotropic tensor or transport eigenvalues reveals that the sign combination of the transport eigenvalues of the symmetric tensor links to the evolution of domainintegral large-scale PV enstrophy and the combination of different signs is most often, meaning the dominance of filamentation process in the SO. In the region with intense anisotropy, the dominant eigenvector tends to be perpendicular to the large-scale PV gradient, indicating an important role of the PV barrier mechanism in the SO transport process. The two distinct decompositions leveraged in our framework generate intriguing and profound results. Under the stationary-transient decomposition, we find a significant stationary contribution and the duality of the topographic effect which can not only anchors stationary structures but also organizes transient motions. Leonard's decomposition, allows us to investigate the collective effects of the standing wave train, cross-scale interaction, and subfilter eddy-eddy interaction on the filtered space-time scale. We emphasize the complete subgrid flux, not the mere Reynolds term, and the LES framework needs to be considered in the subgrid parameterization of the coarse resolution ocean model.

1 **A multifaceted isoneutral eddy transport diagnostic**
2 **framework and its application in the Southern Ocean**

3 **Jingwei Xie^{1,2}, Hailong Liu^{1,2,3*}, and Pengfei Lin^{1,2}**

4 ¹LASG, Institute of Atmospheric Physics, Chinese Academy of Sciences, Beijing 100029, China

5 ²College of Earth and Planetary Sciences, University of Chinese Academy of Sciences, Beijing 100049,
6 China

7 ³Center for Ocean Mega-Science, Chinese Academy of Sciences, Qingdao 266071, China

8 **Key Points:**

- 9 • The Southern Ocean transport processes have intense anisotropy
10 • The stationary and topographic effect is crucial for the subfilter transport
11 • The complete subgrid flux should be considered for the mesoscale eddy scheme

*

Corresponding author: Hailong Liu, lh1@lasg.iap.ac.cn

Abstract

We propose a multifaceted isoneutral eddy transport diagnostic framework that combines the stationary-transient and Leonard’s decomposition in large eddy simulation (LES). We diagnose the subfilter flux, the isotropic transport coefficient, and the anisotropic transport tensor or eigenvalues in the Southern Ocean (SO). The anisotropic tensor greatly reduces the reconstruction error of the subfilter flux because of its ability to distinguish the directionality of dynamic information, especially the topographic effect. A thorough analysis of the anisotropic tensor or transport eigenvalues reveals that the sign combination of the transport eigenvalues of the symmetric tensor links to the evolution of domain-integral large-scale PV enstrophy and the combination of different signs is most often, meaning the dominance of filamentation process in the SO. In the region with intense anisotropy, the dominant eigenvector tends to be perpendicular to the large-scale PV gradient, indicating an important role of the PV barrier mechanism in the SO transport process. The two distinct decompositions leveraged in our framework generate intriguing and profound results. Under the stationary-transient decomposition, we find a significant stationary contribution and the duality of the topographic effect which can not only anchors stationary structures but also organizes transient motions. Leonard’s decomposition, allows us to investigate the collective effects of the standing wave train, cross-scale interaction, and subfilter eddy-eddy interaction on the filtered space-time scale. We emphasize the complete subgrid flux, not the mere Reynolds term, and the LES framework needs to be considered in the subgrid parameterization of the coarse resolution ocean model.

Plain Language Summary

This study applies a spatial coarse-graining method or a 2D spatial filter to define the subfilter or roughly speaking the mesoscale eddying structure as the deviation from the filtered large-scale field. Then, the Reynolds’ temporal average is used to divide the eddying effect into transient and stationary parts. Leonard’s decomposition further allows us to categorize the interactions of eddies versus large-scale flow. Both decompositions together with the flux-gradient relation, which links the eddy flux with the large-scale background gradient through either the isotropic transport coefficient or anisotropic transport tensor, help provide insights into mesoscale eddy transport parameterization design.

1 Introduction

Ocean physical processes with a horizontal spatial scale of approximately 50-500 km or near the first baroclinic Rossby deformation radius are usually called ocean mesoscale motions, including mesoscale eddies and meander structures. Mesoscale motions, which contain more than 80% of the ocean kinetic energy, impact ocean material transport, momentum budget, and interaction with large-scale and submesoscale ocean circulation. Therefore, resolving or at least parameterizing the oceanic mesoscale process in a numerical model is necessary. Since the milestone work of Gent and McWilliams (1990) and Gent et al. (1995) which proposed the GM parameterization scheme to mimic holistic eddy transport effect and the process of releasing the available potential energy by baroclinic instability for application in a coarse resolution ocean model, mesoscale eddy transport parameterization and its accompanying diagnostic methods and theories have been continuously developed over the past three decades, (e.g., McDougall & McIntosh, 1996; Treguier et al., 1997; Visbeck et al., 1997; Dukowicz & Smith, 1997; Griffies et al., 1998; Griffies, 1998; Marshall et al., 1999; McDougall & McIntosh, 2001; Nakamura, 2001; R. Smith & Gent, 2004; Berloff, 2005; Cessi, 2007; Eden & Greatbatch, 2008; Ferrari & Nikurashin, 2010; Marshall et al., 2012; Hallberg, 2013; Bachman & Fox-Kemper, 2013; Bachman et al., 2015; Lu et al., 2016; Mak et al., 2017; Bachman, 2019; Haigh et al., 2020; Groeskamp

et al., 2020; Z. Stanley et al., 2020; Wei & Wang, 2021; Haigh & Berloff, 2021; Haigh et al., 2021a, 2021b, and others)

However, many current parameterization schemes for ocean mesoscale processes and related diagnostic methods have two major defects:

(I) The Reynolds' average method is often used for scale separation so that for any variable c , there is $\bar{\bar{c}} = \bar{c}$, $\overline{c'} = 0$. Nevertheless, the discrete grid algorithm of the numerical model does not necessarily meet the property of the Reynolds average. The grid discretization should be deemed as an implicit filter that one may not know the specific form (Germano et al., 1991; Germano, 1992), which is more likely to be represented by the spatial coarse-graining method. Under the coarse-graining method, $\bar{\bar{c}} \neq \bar{c}$, $\overline{c'} \neq 0$. If assuming a specific scale clearly separating the motion into two untangling parts (for example, the motion with a bimodal spectrum in spectral space), the coarse-graining method can be approximated as Reynolds' average. However, due to the continuity of the energy spectrum of ocean mesoscale processes (Aluie et al., 2018; Buzzicotti et al., 2021), the scale separation hypothesis cannot be well established. Therefore, the complete subgrid flux rather than the mere Reynolds term must be considered for oceanic eddy parameterization. In addition, the Reynolds term only includes the collective contribution of motions smaller than the separation scale (e.g. eddy-eddy interaction) to the larger scale. It does not incorporate the cross-scale or even multi-scale interactions.

(II) Most parameterization schemes only deal with the transient eddy process caused by instabilities, without explicitly involving topographic effect or stationary process which may significantly affect the eddy transport process. Many works (e.g., Treguier & McWilliams, 1990; Rintoul et al., 2001; MacCready & Rhines, 2001; Garabato et al., 2011; A. Thompson & Sallée, 2012; Bischoff & Thompson, 2014; Abernathey & Cessi, 2014; Radko & Kamenkovich, 2017; Youngs et al., 2017; Khani et al., 2019, and others) tried to establish the relationship between stationary phenomena and topography and how topography dynamically force the eddy processes. For example, stationary structures appear downstream of large-scale topographies, which cause zonal inhomogeneity of the flow, make a crucial contribution to the cross-front eddy mass and tracer transport, and both baroclinic instability and barotropic instability could play vital roles in these stationary structure dynamics (Youngs et al., 2017). Most relevant to our study, Lu et al. (2016) showed that stationary eddies would play a non-negligible role in eddy transport and the transport coefficient or tensor in the Southern Ocean (SO) so their effect should be involved in mesoscale eddy parameterization.

Given the above issues, this paper will leverage some large eddy simulation (LES) concepts to diagnose the eddy transport process and form a new perspective on the mesoscale eddy scheme. We believe LES is applicable to the current coarse-resolution climate models which have the typical horizontal resolution near or less than 1° (Hewitt et al., 2020). The grid scale is smaller than the largest mesoscale eddy in the ocean. Therefore, the parameterization of the subgrid process should consider the complete subgrid flux under the LES framework. This paper introduces Leonard's decomposition in LES to discuss the complete subfilter eddy flux and further develop Lu et al. (2016)'s stationary-transient eddy transport diagnostic framework. Using potential vorticity (PV) as a dynamical tracer, we apply this new framework to the realistic ocean data and numerical simulation results of the SO to investigate the characteristics of the subfilter transport in terms of 1) isotropic and anisotropic assumption, 2) stationary-transient decomposition and 3) Leonard's decomposition. This diagnostic framework of eddy transport not only distinguishes the contribution of stationary structure and transient motion in the SO and points out the importance of stationary process or topographic effect, but also looks into the collective effect of the interaction among small eddies, large eddies, and large-scale structures on a given spatio-temporal scale from the perspective of triad interaction, to provide theoretical support for better parameterizing mesoscale eddy process in ocean models. Section 2 will briefly review some basic concepts of the flux-gradient

115 relation, eddy transport tensor, isotropy, and anisotropy. We hybrid the spatial coarse-
 116 graining method and the temporal Reynolds' average to realize the stationary-transient
 117 decomposition, and introduce the so-called Leonard's decomposition in LES with its phys-
 118 ical implication explained from the aspect of the triad interaction and Germano iden-
 119 tity. This section also includes the data and some key processing methods in the calcu-
 120 lation. Section 3 is the diagnosis results, in which Section 3.1 shows the results of sub-
 121 filter eddy PV transport under the stationary-transient decomposition and Leonard's de-
 122 composition, Section 3.2 is the result of isotropic scalar transport coefficient, and Sec-
 123 tion 3.3 is for the anisotropic transport tensor, focusing on the eigenvalue analysis of its
 124 symmetric part. Section 4 is for conclusion and discussion.

125 2 Methods

126 2.1 The flux-gradient relation

127 Starting from the freely evolving dynamic tracer PV equation with the following
 128 form,

$$\frac{\partial q}{\partial t} + \nabla \cdot (\mathbf{u}q) = 0 \quad (1)$$

129 After the scale separation, we obtain the large-scale PV equation,

$$\frac{\partial \{q\}}{\partial t} + \nabla \cdot (\{\mathbf{u}\}\{q\}) + \nabla \cdot \mathbf{F}_{\text{sfs}} = 0 \quad (2)$$

130 where $\{ \}$ represents a certain scale separation operator with a smoothing effect and the
 131 subfilter eddy flux (or transport) is as follows.

$$\mathbf{F}_{\text{sfs}} \equiv \{\mathbf{u}q\} - \{\mathbf{u}\}\{q\} \quad (3)$$

132 In Appendix A, we introduce Germano identity (Germano et al., 1991; Germano, 1992)
 133 to distinguish the two concepts of subgrid and subfilter scale. We also point out in Ap-
 134 pendix A that only when the separation scale of the explicit spatial coarse-graining fil-
 135 ter is sufficiently larger than the scale of the implicit data resolution filter, the subfilter
 136 scale quantity obtained is valid and the subfilter flux would be regarded as the subgrid
 137 flux of a certain coarse-resolution model.

138 Suppose linear relation between the subfilter flux and large-scale PV gradient, namely
 139 adopt the flux-gradient relation as turbulent closure (Taylor, 1922; Vallis, 2017),

$$\mathbf{F}_{\text{sfs}} = -\mathbf{K}\nabla\{q\} \quad (4)$$

140 \mathbf{K} is the eddy transport tensor of second-order, storing the local relation between the
 141 flux and the gradient in physical space. In the z -coordinate, \mathbf{K} is a 3×3 tensor. How-
 142 ever, the mesoscale motion away from the mixing layer is quasi-adiabatic and in prin-
 143 ciple along the neutral density surface or the minimum disturbance surface (McDougall,
 144 1987; Fox-Kemper et al., 2013), so the process can be simplified to 2D. Then \mathbf{K} becomes
 145 a 2×2 tensor.

146 The transport tensor needs not to be symmetric, and one may take symmetric-antisymmetric
 147 decomposition as follows,

$$\mathbf{A} \equiv \frac{1}{2} (\mathbf{K} - \mathbf{K}^T) \quad (5)$$

$$\mathbf{S} \equiv \frac{1}{2} (\mathbf{K} + \mathbf{K}^T) \quad (6)$$

$$\mathbf{F}_{\text{sfs}} = -(\mathbf{A} + \mathbf{S})\nabla\{q\} \quad (7)$$

148 The antisymmetric part \mathbf{A} represents the skew advection along large-scale tracer con-
 149 tours, which corresponds to GM Scheme (Gent & McWilliams, 1990; Gent et al., 1995;
 150 Griffies et al., 1998; Griffies, 1998). The symmetric part \mathbf{S} represents the Fickian-like dif-
 151 fusive process, which corresponds to Redi Scheme (Redi, 1982; Griffies et al., 1998; Griffies,
 152 1998).

153 Further, diagonalize the symmetric tensor to get the eigenvalue matrix $\mathbf{\Lambda}$ and eigen-
 154 vector matrix \mathbf{V} as follows,

$$\mathbf{S} = \mathbf{V}^T \mathbf{\Lambda} \mathbf{V} \quad (8)$$

$$\mathbf{\Lambda} = \begin{bmatrix} \lambda_1 & 0 \\ 0 & \lambda_2 \end{bmatrix} \quad (9)$$

155 We call the larger eigenvalue λ_1 the major eigenvalue, the smaller λ_2 the minor eigen-
 156 value. They represent the diffusion intensity along the major axis (parallel to the direc-
 157 tion of the major eigenvector) and the minor axis (parallel to the direction of the mi-
 158 nor eigenvector), respectively. $\lambda_1 \neq \lambda_2$ means anisotropic diffusion. $\lambda_1 = \lambda_2$ means
 159 isotropic diffusion. If the eddy transport process itself is purely isotropic, then the trans-
 160 port tensor collapses to the scalar coefficient κ and we have the flux-gradient relation

$$\mathbf{F}_{\text{sfs}} = -\kappa \nabla \{q\} \quad (10)$$

161 The transport coefficient here can be understood as the "efficiency" of the eddy trans-
 162 port process, that is, the length of the eddy flux vector standardized by the length of the
 163 large-scale PV gradient, or how much eddy transport can be excited under the background
 164 tracer field gradient of unit intensity.

165 Our diagnostic framework will be used to examine not only the eddy transport it-
 166 self but also the isotropic transport coefficient and the anisotropic transport tensor.

167 2.2 The stationary-transient and Leonard's decomposition

168 This section introduces two independent decomposition methods of the subfilter
 169 flux and its transport tensor: the stationary-transient decomposition and Leonard's de-
 170 composition.

171 Like Lu et al. (2016), we use a 2D boxcar filter for spatial coarse-graining and Reynolds'
 172 temporal average to implement the stationary-transient decomposition. Any quantity
 173 c can be expressed as the sum of large-scale instantaneous background field, subfilter sta-
 174 tionary eddying field, and subfilter transient eddying field, namely

$$c = [c] + c^* = [c] + \bar{c}^* + c'^* \quad (11)$$

175 where $[c]$ is for the spatial smoothed field; \bar{c} is for the time-averaged field; $c^* = c - [c]$
 176 is for the spatial subfilter eddying field, namely the original field minus the spatial smoothed
 177 field; $c' = c - \bar{c}$ is for the temporal eddying field, namely the original field minus the
 178 time-averaged field. The spatial subfilter eddying field c^* contains the stationary eddy-
 179 ing field \bar{c}^* and the transient eddying field c'^* . Note that the filter scale involved in this
 180 paper is 1° - 3° and inside the spectral range of the ocean mesoscale process. Although
 181 closely related, the subfilter scale cannot be completely equivalent to the oceanic mesoscale.
 182 If the mesoscale eddies are divided into large eddies and small eddies, the subfilter scale
 183 in this paper can be regarded as the ensemble of small eddies plus part of large eddies,
 184 and the filter scale can be regarded as the remaining part of large eddies plus large-scale
 185 field.

186 Replace the scale separation operator $\{ \}$ in in Eq.1 with $\overline{[]}$, the subfilter PV flux
 187 becomes the following form

$$\mathbf{F}_{\text{sfs}} \equiv \overline{[\mathbf{u}q]} - [\overline{\mathbf{u}}][\bar{q}] \quad (12)$$

188 We now introduce the classical Leonard's decomposition in LES to decompose the
 189 subfilter flux.

$$\mathbf{F}_{\text{sfs}} = (\overline{[\mathbf{u}][q]}) - [\bar{\mathbf{u}}][\bar{q}] + (\overline{[\mathbf{u}]q^*}) + [\mathbf{u}^*][q] + (\overline{[\mathbf{u}^*q^*]}) \quad (13)$$

190 The three terms in brackets on the right side of the equation are the Leonard term, Cross
 191 term, and Reynolds term, respectively (Leonard, 1974; Clark, 1977; Clark et al., 1979;
 192 Speziale, 1985; Germano, 1992; Fox-Kemper & Menemenlis, 2008; Anderson & Domaradzki,
 193 2012). These three terms represent three categories of microstructures in the spectral
 194 space in terms of triad interaction (see Appendix B for details): 1) the Leonard term (com-
 195 bined with the large-scale transport term in the second term on the left of Eq.1) incor-
 196 porates the collective effect of the triad interaction larger than the separation scale, which
 197 is defined as filtered-filtered or resolved-resolved interaction (including large-scale pro-
 198 cess, part of large-eddy versus large-scale flow interaction and part of large-eddy versus
 199 large-eddy interaction); 2) The Cross term represents the collective effect of the cross-
 200 scale interaction between the filtered and subfilter quantities on the filtered scale evo-
 201 lution, which is defined as filtered-subfilter or resolved-subgrid interaction (including eddy
 202 versus large-scale flow interaction, small-eddy versus large-eddy interaction and part of
 203 large-eddy versus large-eddy interaction); 3) The Reynolds term represents the collec-
 204 tive effect on the filtering scale evolution caused by the process that occurs purely less
 205 than the separation scale, which is defined as subfilter-subfilter or subgrid-subgrid in-
 206 teraction (including the remaining eddy-eddy interaction that can be resolved by the data
 207 resolution). The collective effect here refers to the statistical effect on both large time
 208 and spatial scales. The essential difference between the three terms is that their triad
 209 elements have 0, 1, and 2 subfilter wave vectors, respectively. Since we do not choose the
 210 spectral truncated filter, the so-called "separation scale" above should be regarded as
 211 a generalized "separation scale or wavenumber interval" near the characteristic scale or
 212 wavenumber of the filter. In this interval, from larger scale to smaller scale, the propor-
 213 tion of subfilter components increases and tends to 1, and the proportion of filtered com-
 214 ponents gradually tends to zero. In addition, when the filter scale increases, the filtered
 215 part accommodates fewer eddying processes, so the Leonard term tends to be the pure
 216 large-scale process. Despite this expected dependence, our results will show that the qual-
 217 itative behavior of Leonard's decomposition is not sensitive to the filter scale in the range
 218 we discussed.

219 Combine the stationary-transient decomposition with Leonard's decomposition, we
 220 have

$$\begin{aligned} \mathbf{F}_{\text{Lnr,d,t1}} &\equiv \overline{[\mathbf{u}][q]} - [\mathbf{u}][q] \\ &= ((\overline{[\bar{\mathbf{u}}][\bar{q}]} - [\bar{\mathbf{u}}][\bar{q}]) + (\overline{[\mathbf{u}'][q']})) \\ &= \mathbf{F}_{\text{Lnr,d,stt}} + \mathbf{F}_{\text{Lnr,d,trs}} \end{aligned} \quad (14)$$

$$\begin{aligned} \mathbf{F}_{\text{Crs,t1}} &\equiv \overline{[\mathbf{u}]q^*} + [\mathbf{u}^*][q] \\ &= ((\overline{[\bar{\mathbf{u}}]q^*} + [\bar{\mathbf{u}}^*][q]) + (\overline{[\mathbf{u}']q'^*} + [\mathbf{u}^{*'}][q'])) \\ &= \mathbf{F}_{\text{Crs,stt}} + \mathbf{F}_{\text{Crs,trs}} \end{aligned} \quad (15)$$

$$\begin{aligned} \mathbf{F}_{\text{Rynlds,t1}} &\equiv \overline{[\mathbf{u}^*q^*]} \\ &= \overline{[\bar{\mathbf{u}}^*q^*]} + \overline{[\mathbf{u}^{*'}q'^*]} \\ &= \mathbf{F}_{\text{Rynlds,stt}} + \mathbf{F}_{\text{Rynlds,trs}} \end{aligned} \quad (16)$$

221 The first terms on the right of the above three equations represent the stationary com-
 222 ponent, and the seconds are the transient ones. We use t1, stt, and trs to represent the

223 total, stationary and transient components, respectively. The stationary and transient
 224 subfilter flux can be expressed as

$$\mathbf{F}_{\text{sfs, stt}} \equiv ([\overline{[\mathbf{u}][q]}] - [\overline{\mathbf{u}}][\overline{q}] + ([\overline{[\mathbf{u}]\overline{q}^*}] + [\overline{\mathbf{u}^*}][\overline{q}]) + ([\overline{\mathbf{u}^*}\overline{q}^*]) \quad (17)$$

$$\mathbf{F}_{\text{sfs, trs}} \equiv ([\overline{[\mathbf{u}'] [q']}]) + ([\overline{[\mathbf{u}'] q'^*}] + [\overline{\mathbf{u}'^*} [q']]) + ([\overline{\mathbf{u}'^* q'^*}]) \quad (18)$$

225 The stationary part is composed of time-averaged quantities. It captures the time-invariant
 226 or slowly-varying imprint, which is forced by setting system boundary conditions (such
 227 as topography and air-sea flux) and hyperparameters (such as the Coriolis parameter f
 228 and β). The transient part measures the collective effect of the evolving dynamic adjust-
 229 ment processes around the stationary structure in the system.

230 Through the flux-gradient relationship, we can obtain the transport tensor for ev-
 231 ery part,

$$\mathbf{F}_{\text{sfs}} = -\mathbf{K}^{\text{sfs}} \nabla [\overline{q}] \quad (19)$$

$$\mathbf{F}_{\text{stt}} = -\mathbf{K}^{\text{stt}} \nabla [\overline{q}], \quad \mathbf{F}_{\text{trs}} = -\mathbf{K}^{\text{trs}} \nabla [\overline{q}] \quad (20)$$

$$\mathbf{F}_{\text{Lnr}} = -\mathbf{K}^{\text{Lnr}} \nabla [\overline{q}], \quad \mathbf{F}_{\text{Crs}} = -\mathbf{K}^{\text{Crs}} \nabla [\overline{q}], \quad \mathbf{F}_{\text{Rynlds}} = -\mathbf{K}^{\text{Rynlds}} \nabla [\overline{q}] \quad (21)$$

232 We also have the expressions of the transport tensors,

$$\mathbf{K}^{\text{sfs}} = \mathbf{K}^{\text{stt}} + \mathbf{K}^{\text{trs}} = \mathbf{K}^{\text{Lnr}} + \mathbf{K}^{\text{Crs}} + \mathbf{K}^{\text{Rynlds}} \quad (22)$$

233 namely, the transport tensor can also be decomposed by the stationary-transient and Leonard's
 234 decomposition. So far, we have established a multifaceted eddy transport diagnosis frame-
 235 work using both the stationary-transient and Leonard's decomposition as well as whether
 236 isotropic or not. This framework helps investigate the contribution of the stationary and
 237 transient effects and different categories of triad interaction under Leonard's decompo-
 238 sition to the eddy transport in the SO.

239 2.3 Data and processing method

240 The main results of this paper are based on the five-day average SOSE eddy-permitting
 241 data (Mazloff et al., 2010) with a horizontal resolution of $1/6^\circ$ in 2008. Data from an
 242 eddy-rich quasi-global model LICOM2 (LASG/IAP Climate system Ocean Model) with
 243 a horizontal resolution of $1/10^\circ$ is used for validation (see Yu et al. (2012) for the sim-
 244 ulation setting). We take the data in the 63rd model year, which is well spinup. The study
 245 area is south of 25°S . In this paper, the temporal Reynolds' average is the annual av-
 246 erage, and the spatial coarse-graining adopts the boxcar filter with a fixed size of 2° . We
 247 will also show some results of 1° and 3° to discuss the sensitivity to the selected sepa-
 248 ration scale, but the major discussion is for 2° . When close to the boundary, the filter
 249 size remains unchanged, and the missing values are set to zero to participate in the fil-
 250 tering, so the filtered boundary also becomes fuzzy. This method performs well in terms
 251 of energy conservation and commutes with differential operators (Buzzicotti et al., 2021),
 252 and its discretization expression is as follows,

$$[c]_{mn} = \frac{1}{num} \sum_{i=m-ir}^{m+ir} \sum_{j=n-ir}^{n+ir} w_{ij} c_{ij}, \quad num = (2ir + 1)^2 \quad (23)$$

253 ir is the grid number of half filter size, and w_{ij} is the area weight.

254 The multifaceted diagnostic framework of this paper needs to be carried out on the
 255 neutral density surface. We use the topobaric surface to estimate the neutral surface,
 256 which is highly accurate (Stanley, 2019). We choose the surface with a neutral density
 257 of $36.8kg/m^3$ for discussion because it has outcrop areas near the Antarctic continent
 258 only a few times a year. In most areas north of $60^\circ S$, its depth is about $1500\pm 1000m$,
 259 enabling us to reduce the influence of the diabatic process in the mixing layer. The re-
 260 sults of flux and transport tensor in other layers are qualitatively consistent. In addi-
 261 tion, the potential density σ_2 can also be used to estimate the neutral density, which is
 262 significantly different from the results of the topobaric surface in places with steep isopy-
 263 cnal slope (such as the ACC core) near the outcrop area. However, the spatial distribu-
 264 tion of physical quantities in other places is qualitatively consistent. To reduce the amount
 265 of calculation, we only processed higher resolution LICOM data on the σ_2 plane. The
 266 velocity field under this framework is the velocity projected from the z-coordinate to the
 267 neutral plane. The dynamic tracer PV, $q = fN^2/g = -\frac{f}{\rho} \frac{\partial \rho}{\partial z}$, is firstly calculated in
 268 the z-coordinate and then interpolated into the neutral coordinate. Appendix C gives
 269 a brief example of our interpolation algorithm. The subsequent filtering and gradient op-
 270 erations are carried out on the neutral plane.

271 On the neutral plane, the total subfilter PV flux is calculated first, and then the
 272 components of the flux are obtained through the stationary-transient and Leonard's de-
 273 composition. Then the corresponding transport tensors or coefficients are estimated through
 274 the flux-gradient relation. Finally, the transport tensors are decomposed into symmet-
 275 ric and antisymmetric parts, and the eigenvalues and eigenvectors of the symmetric ten-
 276 sor are calculated. Unlike the multi-tracer method (Bachman et al., 2015), only one dy-
 277 namic tracer is used here. We carried out the least-square regression of neighboring sam-
 278 ples to solve the underdetermined problem in estimating the transport coefficient or ten-
 279 sor. Appendix C describes how the approach is implemented. Specifically, solving the
 280 transport tensor is equivalent to solving the following binary linear least-square regres-
 281 sion problems,

$$\begin{bmatrix} f^x \\ f^y \end{bmatrix} = \begin{bmatrix} K_{xx} & K_{xy} \\ K_{yx} & K_{yy} \end{bmatrix} \begin{bmatrix} [\bar{q}]_x \\ [\bar{q}]_y \end{bmatrix} \rightarrow \begin{cases} f^x = K_{xx}[\bar{q}]_x + K_{xy}[\bar{q}]_y \\ f^y = K_{yx}[\bar{q}]_x + K_{yy}[\bar{q}]_y \end{cases} \quad (24)$$

282 f^x and f^y are the zonal and meridional subfilter PV flux, respectively. The estimation
 283 of the isotropic coefficient is also similar and becomes linear least-square regression be-
 284 tween the length of flux vector and the length of the large-scale PV gradient vector.

285 3 Result

286 3.1 Meridional subfilter PV flux

287 3.1.1 The stationary-transient decomposition

288 As show in Figure C1a The large value area of the meridional subfilter PV flux is
 289 concentrated in the south of the domain and the eastern side of the continent or sub-
 290 marine plateau (Figure C1a and C1g). The large value zone near the Antarctic conti-
 291 nent reflects the influence of non-conservative processes such as sea-ice dynamics, and
 292 outcropping of the neutral surface or mixing layer effect. Since our framework is designed
 293 for inner ocean quasi-adiabatic motion, we will not discuss this more but blame it on the
 294 inapplicability of our diagnostic method there. The large value zones on the eastern side
 295 of large-scale topography have clear physical significance. They are contributed mainly
 296 by the stationary flux (Figure C1b), so it reflects the anchoring effect of topography on
 297 the eddy transport pattern. In addition, the mid-ocean ridge imprint a clear pattern on
 298 both stationary and transient subfilter flux, which is manifested in the arc-shaped mag-
 299 nitude mutation area near $150^\circ E$ - $150^\circ W$, $60^\circ S$ and $10^\circ E$ - $35^\circ E$, $50^\circ S$ and the northward
 300 extension of the large value area at $80^\circ E$, $150^\circ E$ and $10^\circ W$. Our results reflect the du-
 301 ality of the topographic effect, that is, the large-scale topography not only anchors sta-
 302 tionary structures of the flux field but also organizes transient adjustment processes nearby.

303 This is consistent with previous studies using idealized models or observation data to di-
 304 agnose eddy kinetic energy, eddy momentum flux, eddy buoyancy flux, and other eddy
 305 tracer fluxes (e.g., A. Thompson & Sallée, 2012; A. Thompson & Garabato, 2014; Bischoff
 306 & Thompson, 2014; Youngs et al., 2017). In addition, although the results of boxcar fil-
 307 ters of different sizes are qualitatively consistent (Figure S1), the separation scale would
 308 affect the relative contribution of the stationary and transient components to the sub-
 309 filter flux (Figure C3). The larger the filter scale, the stronger the contribution of the
 310 stationary part and the weaker the transient part. This is because the high-pass field with
 311 a larger filter scale contains more large-scale information. The dominance of the station-
 312 ary part increasing with the filter size reflects that the scale of the transient process is
 313 smaller than the scale of the stationary structure formed by the anchoring effect of the
 314 topography. An example is that the quasi-stationary meander in the SO is often larger
 315 than the transient mesoscale eddy (Williams et al., 2007; Chapman et al., 2015).

316 *3.1.2 Leonard’s decomposition*

317 This section investigates the Leonard term, Cross term, and Reynolds term of the
 318 subfilter flux under Leonard’s decomposition. From the horizontal distribution and prob-
 319 ability density function (PDF) of meridional PV flux (Figure C2 and C3), we find large
 320 a Leonard term and Cross term with a positive and negative staggered wave train dis-
 321 tribution in the domain. However, there is a violent offset between the two, which makes
 322 the sum term one order of magnitude smaller than the individual term but still stronger
 323 than the Reynolds term holistically (Figure C3). Similarly, when Galmarini et al. (2000)
 324 used the high-frequency time series of atmospheric variables for time coarse-grained anal-
 325 ysis, they also observed significant Leonard term and Cross term and their partial can-
 326 cellation. Speziale (1985) pointed out that the complete subfilter eddy flux, the sum of
 327 the Leonard term and Cross term, and the individual Reynolds term all satisfy Galilean
 328 invariance, but the form of the individual Leonard term or Cross term is not Galilean
 329 invariant. Therefore, he suggested that the Leonard and Cross term should be param-
 330 eterized together, and the Reynolds term should be parameterized separately. We are
 331 not sure whether the offset here is related to the breaking of Galilean invariance. Most
 332 existing mesoscale eddy parameterization schemes are theoretically derived based on Reynolds’
 333 average. Only the Reynolds term is included, and the other two terms under Leonard’s
 334 decomposition are missed. The results here at least show the importance of considering
 335 a complete subgrid flux, which incorporates the resolved-resolved, resolved-subgrid, and
 336 subgrid-subgrid interactions, and selecting appropriate parameterization form for differ-
 337 ent processes when designing eddy transport parameterization.

338 In addition, these three terms are dominated by the stationary part, and the off-
 339 set between the Leonard and Cross term is mainly from their stationary components.
 340 From Eq.14 of the Leonard term, one may also regard it as a standing wave with asym-
 341 metric amplitude. The geographical position of the peaks, troughs, and zeroes is quasi-
 342 fixed. The stationary Leonard term is the spatial distribution of a stationary background
 343 state with systematic amplitude shift relative to the zero axis just like a canvas with in-
 344 homogeneous background color. The transient Leonard term is the collective effect of
 345 the disturbances that only time-dependent modifies the amplitude of the standing wave.
 346 The stationary Cross term may be understood as a tendency to excite the cross-scale or
 347 multi-scale interaction in specific geographical locations through many possible mech-
 348 anisms. For example, the western boundary flow is the graveyard of eddies (Zhai et al.,
 349 2010). The eddy may also tend to extract energy from the background flow at a specific
 350 location near topography (Abernathey & Cessi, 2014; A. Thompson & Garabato, 2014).
 351 Special geometric shapes and configuration of eddy and background flow to realize cross-
 352 scale energy conversion (Waterman & Lilly, 2015; Youngs et al., 2017), which might repet-
 353 itively occur someplace, would also contribute to the stationary Cross term.

Further comparing the results of SOSE with higher resolution LICOM simulation (Figure S2), the spatial distribution of the Leonard or Cross term from different data is qualitatively consistent in terms of wavelength and geographical distribution of the wave train structure. Therefore, one speculation is that these two reflect the system's fingerprint under the current topographic and climate state or model setting. Since the stationary part dominates these two, we offer an interpretation of the wave train structure that macro-conditions of the system, such as all its boundary conditions (e.g. topography and air-sea flux) and hyperparameters (for example, f and β), can decisively stimulate the large-scale process, eddy versus large-scale interaction and small eddy versus large eddy interaction encompassed in the Leonard and cross term with a definite geographical distribution.

3.2 The isotropic transport coefficient

3.2.1 *The stationary-transient decomposition*

The large values of the isotropic subfilter transport coefficient (Figure C1d) are mainly in the vigorous flow areas, such as the Antarctic Circumpolar Current (ACC), the Agulhas retroflection, and the Malvinas current. Under the stationary-transient decomposition (Figure C1def), the stationary coefficient dominates in most places, and the large transient coefficient mainly concentrates in the most energetic flow area such as the ACC. This is a surprising result. Although some studies, for instance, Lu et al. (2016) has discovered the significance of the stationary part in the transport process, we uncover for the first time that the stationary effect would dominate the transport process when the complete subfilter flux is considered, so a complete mesoscale eddy scheme should never omit the stationary effect. Large-scale topography often excites strong subfilter transport coefficients downstream of the local flow, such as the eastern side of the Kerguelen plateau and Campbell Plateau, the Malvinas current, and the southwest side of the African continent which is equivalent to the downstream of the Agulhas retroflection. In addition, the coefficient also has the structure of several banded weak value areas, which is particularly obvious in the stationary part at 100°E-160°W. This structure may be related to the mid-ocean ridge because its orientation is consistent with the mid-ocean ridge. The topographic type of large-scale and undulating zonal ridges can form an obstacle to eddy mixing by locally strengthening the jet (A. F. Thompson, 2010). In observation data or realistic model runs, the role of topography on the flow field is a complex, multi-scale problem. This work only qualitatively sheds some light on the influence of topography on the eddy transport process. Future work will comprehend how the specific topographic configuration drives the transport under our diagnostic framework by carrying out idealized numerical experiments with a simplified model setting. In addition, the size of the boxcar filter affects the relative contribution of the stationary and transient components to the subfilter transport coefficient: the larger the filter scale, the more the contribution of the stationary part (Figure C5).

3.2.2 *Leonard's decomposition*

The relative magnitude among the three terms of the subfilter eddy transport coefficient is consistent with the subfilter flux result when Leonard's decomposition is adopted. The Leonard and Cross term is one order of magnitude larger than the Reynolds term, and they partially offset each other but the sum of the Leonard and Cross term is still more intense than the Reynolds term (Figure C5). The Leonard term and Cross term achieve high intensity on the ACC core and its northern flank, while their magnitude drops drastically on the southern side of ACC (Figure C4). Compared with Figure C1g, the continuous submarine plateau, mid-ocean ridge between 50°S and 70°S shape the boundary of different levels of intensity of the Leonard and Cross transport coefficient. In addition, although the subfilter flux and the Reynolds transport coefficient are small in the gyre area (such as 40°S in the South Pacific) where the flow is relatively slow and EKE

405 is not that vigorous, the Leonard and Cross coefficient reach a decent level of intensity.
 406 This means the standing wave effect and cross-scale interaction represented by the Leonard
 407 and Cross transport coefficients are of high efficiency influencing tracer transport dynam-
 408 ics. Classical schemes are often based on Reynolds' average assumption, so they merely
 409 handle the effect of the Reynolds term, not the full transport process. The Leonard and
 410 Cross effects are overwhelming in areas where mesoscale eddy activity is not abundant,
 411 and they should be taken into account when parameterizing.

412
 413 Although the diagnosis of the isotropic transport coefficient is instructive, the trans-
 414 port coefficient in this paper attempts to establish the association between the length
 415 of large-scale PV gradient and flux. In its mathematical essence, the isotropic form blends
 416 information from different directions. That leads to a dramatic error of meridional PV
 417 flux reconstructed by the isotropic transport coefficient (Figure C6bc), and the failure
 418 to capture the stationary PV flux field pattern inscribed by the topographic anchoring
 419 effect. However, if the anisotropic transport tensor is used, the reconstruction error can
 420 be greatly reduced (Figure C6de). As a second-order tensor, the anisotropic transport
 421 tensor stores more critical dynamic connections, especially the topographic effect exerted
 422 in different orientations, than the isotropic coefficient which is a zero-order tensor. There-
 423 fore, we will discuss the anisotropic framework in the next section.

424 **3.3 The anisotropic transport tensor**

425 The anisotropic transport tensor can be decomposed into a symmetric and anti-
 426 symmetric tensor. The symmetric part represents the Fickian-like eddy diffusion pro-
 427 cess, and the antisymmetric part represents the advective process of skew flux (Griffies
 428 et al., 1998; Griffies, 1998). Although our diagnostic framework can generate the results
 429 of all relevant components and elements of the transport tensor, we only focus on the
 430 eigenvalues of the symmetric tensor (hereinafter referred to as the transport eigenval-
 431 ues). The results of the antisymmetric part are given in Figure S8, but will not be dis-
 432 cussed in this manuscript.

433 **3.3.1 The transport eigenvalues**

434 The transport eigenvalue has features qualitatively consistent with the transport
 435 coefficient above, including: 1) the large value of the subfilter transport eigenvalue is con-
 436 centrated in the vigorous flow region, and the contribution of the stationary part is stronger
 437 than that of the transient part (Figure C7 and C8). 2) The eigenvalue intensity of the
 438 Leonard and cross terms is at least one order of magnitude greater than that of Reynolds
 439 terms (Figure C8), but the eigenvalues of these two terms do not seem to offset. In fact,
 440 when considering the subfilter flux and transport coefficient, the coordinate axes of the
 441 vector projection are meridional and zonal. However, in the eigenvalue analysis, the base
 442 vectors are the local major eigenvector and minor eigenvector, so the eigenvalues of the
 443 Leonard and cross term do not have additivity. 3) The Leonard and Cross term are com-
 444 pletely dominated by the stationary part (Figure S4, S5 and C8), and the stationary and
 445 transient part of the Reynolds term are nearly in the same order of magnitude (Figure
 446 S3 and C8). As the spatial separation scale decreases, the importance of the transient
 447 part increases (Figure S7); When the eddy-rich LICOM data is adopted for a fixed spa-
 448 tial separation scale, the importance of the transient part also increases (Figure S6). 4)
 449 The transport eigenvalue intensities of the Leonard and cross terms have a distinct bound-
 450 ary near 60°S. As mentioned above, this boundary is related to the separation of bot-
 451 tom topography. There is a decent level of eigenvalue intensity where the flow is rela-
 452 tively weak in the northern flank of ACC.

453 In addition to the above features, the transport eigenvalues can better show the
 454 anchoring effect of the topography, especially the minor eigenvalues of the stationary Reynolds
 455 term are strengthened on the eastern side of all large-scale topography (Figure S3e). This
 456 indicates that 1) the response of the transport process to topographic forcing has dis-
 457 tinct directionality, and 2) the anisotropic transport tensor can distinguish the physi-
 458 cal relationship in different directions.

459 We next discuss the unique characteristics of the transport eigenvalue, that is, the
 460 three combinations of the transport eigenvalues, including 1) positive major eigenvalue
 461 and negative minor eigenvalue (major+, minor-), 2) positive eigenvalues (major+, mi-
 462 nor+), and 3) negative eigenvalues (major-, minor-). We will try to uncover the phenom-
 463 ena in realistic data and the physical implication.

464 From the large-scale PV equation Eq.2, we can obtain the large-scale PV enstro-
 465 phy equation,

$$\frac{\partial}{\partial t} \left(\frac{\{q\}^2}{2} \right) + \{q\} \nabla \cdot (\{\mathbf{u}\}\{q\}) + \nabla \cdot (\{q\}\mathbf{F}_{\text{sfs}}) - \mathbf{F}_{\text{sfs}} \cdot \nabla \{q\} = 0 \quad (25)$$

466 We can further get the domain-integrated equation and focus on the terms incorporat-
 467 ing the subfilter process,

$$\frac{\partial}{\partial t} \int_{\Omega} \frac{\{q\}^2}{2} d\Omega \sim - \int_{\Omega} \nabla \cdot (\{q\}\mathbf{F}_{\text{sfs}}) d\Omega + \int_{\Omega} \mathbf{F}_{\text{sfs}} \cdot \nabla \{q\} d\Omega \quad (26)$$

$$Z = \int_{\Omega} \frac{\{q\}^2}{2} d\Omega \quad (27)$$

468 Here Z is the domain integral of large-scale PV enstrophy, hereinafter referred to as large-
 469 scale enstrophy. Under the condition that the boundary value is zero (the coarse-graining
 470 method in this paper makes the large-scale PV asymptotically close to zero at the do-
 471 main boundary), the first term on the right of Eq.26 is zero, then we obtain the follow-
 472 ing relation,

$$\frac{\partial Z}{\partial t} \sim \int_{\Omega} \mathbf{F}_{\text{sfs}} \cdot \nabla \{q\} d\Omega = - \int_{\Omega} \mathbf{K} \nabla \{q\} \cdot \nabla \{q\} d\Omega = - \int_{\Omega} \mathbf{S} \nabla \{q\} \cdot \nabla \{q\} d\Omega \quad (28)$$

473 Note that the antisymmetric tensor \mathbf{A} is eliminated because its skew flux is perpendic-
 474 ular to the large-scale PV gradient. For the interaction of symmetric tensor \mathbf{S} and PV
 475 gradient vector, we consider coordinate rotation to transform from local $x - y$ coordi-
 476 nate (i.e. the base vector is the local zonal and meridional unit vector) to local charac-
 477 teristic coordinate $v_1 - v_2$ (i.e. the base vector is two local eigenvectors),

$$\mathbf{S} \nabla \{q\} = \begin{bmatrix} S_{xx} & S_{xy} \\ S_{yx} & S_{yy} \end{bmatrix}_{x,y} \begin{bmatrix} r_x \\ r_y \end{bmatrix}_{x,y} \quad (29)$$

$$= \begin{bmatrix} \lambda_1 & 0 \\ 0 & \lambda_2 \end{bmatrix}_{v_1,v_2} \begin{bmatrix} r_{v_1} \\ r_{v_2} \end{bmatrix}_{v_1,v_2} = \begin{bmatrix} \lambda_1 r_{v_1} \\ \lambda_2 r_{v_2} \end{bmatrix}_{v_1,v_2} \quad (30)$$

478 r_x and r_y are the projections of the large-scale PV gradient vector in the x and y direc-
 479 tion respectively, and r_{v_1} and r_{v_2} are the projections of the gradient vector in the ma-
 480 jor and minor eigenvector direction, respectively. Note that the tensor and vector them-
 481 selves are invariant under a coordinate transformation. The first and last expressions rep-
 482 resent exactly the same objective entity, but their projection's expression changes in dif-
 483 ferent coordinates.

484 Finally, we obtain the eigenvalues' contribution to large-scale enstrophy as

$$\frac{\partial Z}{\partial t} \sim - \int_{\Omega} \mathbf{S} \nabla \{q\} \cdot \nabla \{q\} d\Omega = - \int_{\Omega} (\lambda_1 r_{v_1}^2 + \lambda_2 r_{v_2}^2) d\Omega \quad (31)$$

485 (major+, minor-) represents the attenuation of the large-scale PV enstrophy in the ma-
 486 jor characteristic direction and the enhancement of enstrophy in the minor direction, cor-
 487 responding to the vortex filamentation process (Haigh et al., 2020; Ledwell et al., 1998);
 488 (major+, minor+) weakens the large-scale PV enstrophy in both characteristic direc-
 489 tions, which means a pure sink of the enstrophy, and the anisotropy implies that the rates
 490 in different directions are different; (major-, minor-) enhances the large-scale PV enstro-
 491 phy, meaning a pure source of enstrophy. (major+, minor-) is the most common case (Fig-
 492 ure C7). The joint PDF of eigenvalues is mainly concentrated in the fourth quadrant (Fig-
 493 ure C8), and the occurrence frequency is more than 70% (Figure C9a), which means that
 494 the vortex filamentation process is dominant in the subfilter transport process in the SO.
 495 This result is consistent with Haigh et al. (2020); Haigh and Berloff (2021); Haigh et al.
 496 (2021b); Kamenkovich et al. (2021), but their results are obtained from studying instan-
 497 taneous transport eigenvalues of a closed ocean basin. The other two cases' frequency
 498 under different terms has different behavior (Figure C9a), specifically (1) the frequency
 499 of (major+, minor+) of total subfilter, total Reynolds, stationary subfilter, stationary
 500 Reynolds, and all transient terms are higher than that of (major+, minor-), indicating
 501 that the pure sink area of the large-scale PV enstrophy caused by the transient process
 502 and subfilter-subfilter interaction in the SO is larger than the pure source area; (2) The
 503 frequency of total and stationary Leonard and cross terms is almost the same, indicat-
 504 ing that the pure source area and pure sink area of the large-scale PV enstrophy formed
 505 by standing wave effect and stationary cross-scale interaction in the SO are nearly the
 506 same.

507 To explore the anisotropy of transport eigenvalues, unlike Rypina et al. (2012) and
 508 Bachman et al. (2020) which used tensor ellipses to visualize local anisotropy, we cal-
 509 culate the logarithm of the absolute value of the ratio of major and minor eigenvalues
 510 under all three eigenvalue combinations as a measure of anisotropy and focus on their
 511 statistical characteristics. In Figure C9b, we use boxplots to show their mean, 1-fold stan-
 512 dard deviation of the mean, and the upper and lower 5% quantiles. For the case of (ma-
 513 jor+, minor+) (red box), the mean anisotropy of all terms is near 1, and the upper 5%
 514 quantile is at least 2, which indicates the major eigenvalue is at least one order of mag-
 515 nitude or even more than two orders of magnitude larger than the minor eigenvalue and
 516 dominates the degree of anisotropy in a considerable part of the domain. For the most
 517 common case of (major+, minor-) (green box), the mean anisotropy of all terms is near
 518 0, and the 1-fold standard deviation of the mean falls within ± 1 , indicating the magni-
 519 tude of major and minor eigenvalues is close to each other. For the case of (major-, minor-
 520) (blue box), the mean anisotropy of all terms is less than -1, and the lower 5% quan-
 521 tile significantly breaks through -2, which indicates the minor eigenvalues dominate the
 522 degree of anisotropy. In conclusion, the anisotropy of the eddy transport process in the
 523 SO is ubiquitous and drastic.

524 As for different terms, the boxplot of total and stationary Leonard and Cross terms
 525 is highly symmetric about the zero line; that is, the red box and blue box of Lnr-d-ttl,
 526 Crs-ttl, Lnr-d-stt, Crs-stt are symmetric about the zero line, while the green box itself
 527 is symmetrical about the zero line. The upper 5% quantile of the other eight terms with
 528 (major+, minor+) (the top of the red box) is slightly closer to the zero line than the lower
 529 5% quantile of (major-, minor-), indicating that the anisotropy in the pure source of en-
 530 strophy formed by the standing wave effect and stationary cross-scale interaction is slightly
 531 greater than that in the pure sink. In addition, the mean value of the other eight terms
 532 with (major+, minor-) is greater than zero, and their upper 5% quantile is more distant
 533 from the zero line than their lower 5% quantile, indicating that the transient process,
 534 eddy-eddy interaction and vortex filamentation process in the SO slightly dissipate the
 535 large-scale PV enstrophy holistically.

536

3.3.2 *The transport characteristic direction*

537

538

539

540

541

542

543

544

545

546

547

548

549

550

551

552

553

554

555

556

557

This section will discuss the eigenvectors of the symmetric transport tensor. Since the major eigenvalue specified by the algorithm is always greater than or equal to the minor eigenvalue, when the major and minor eigenvalues are both negative, the major eigenvector is not in the dominant direction. Therefore, we select the major eigenvector where the absolute ratio of major and minor eigenvalues is greater than a threshold value α , and the minor eigenvector where the absolute ratio of major and minor eigenvalues is less than $1/\alpha$, to synthesize the truly dominant characteristic direction with strong anisotropy. We calculate the PDF of the angle between the dominant direction and the vector of the large-scale topographic slope, PV gradient, and velocity, as shown in Figure C10, and α is taken as 5. We find the dominant characteristic direction has a strong tendency to be perpendicular to the large-scale PV gradient and parallel to the large-scale velocity vector, and a weak tendency to be perpendicular to the large-scale topographic slope. This is consistent with the results diagnosed by Bachman et al. (2020) with global model data, indicating that the PV gradient barrier and shear dispersion mechanism are critical for the maintenance of anisotropy (Young et al., 1982; S. Smith, 2005; Srinivasan & Young, 2014; Bachman et al., 2020). We further explore the influence of the threshold α . In Figure C11, we investigate the angle between the dominant characteristic direction and the PV gradient when α is 2, 5, 10, and 20. With more intense anisotropy, the perpendicular tendency of the dominant characteristic direction and both its stationary and transient parts are significantly enhanced, with the stationary part's enhancement more dramatic.

558

559

560

561

562

563

564

565

566

Similarly, we can obtain the angles in the weak anisotropy area by giving the threshold γ , as shown in Figure C10, and set $\gamma = 2$. The angle between the dominant characteristic direction and the topographic slope or the velocity vector is almost random and evenly distributed, but the angle between the dominant characteristic direction and the PV gradient peaks near 50° . As the threshold γ (Figure C11) decreases or the isotropy increases, the PDF of the angle between the dominant direction and the PV gradient tends to be symmetrically distributed with 45° as the central peak. These phenomena mean no dominant mechanism among which we have studied can decide the eigenvector when the process is quasi-isotropic.

567

568

569

570

571

The tendency of the stationary dominant eigenvector to be perpendicular to the PV gradient or parallel to the velocity vector is much stronger than the transient component. But there is only a weak orthogonal tendency between the stationary dominant direction and the topographic slope. So it seems that the direct effect of topography is exerted more on the magnitude of transport-related quantities, not their direction.

572

573

574

575

576

577

Above we confirm the relationship between the dominant characteristic direction and the PV gradient under the constraint of geostrophic dynamics. At the same time, we further point out that in the region with high transport anisotropy, the dominant characteristic direction is more likely to be perpendicular to the PV gradient, indicating that the PV barrier mechanism would have a crucial impact on the eddy transport process (Ferrari & Nikurashin, 2010; Srinivasan & Young, 2014; Bachman et al., 2020).

578

4 Summary

579

580

581

582

583

584

585

This paper combines the stationary-transient decomposition and Leonard's decomposition in LES to form a multifaceted diagnostic framework for the eddy transport process applied in the SO. We not only distinguish the contribution of stationary structure and transient motion and validate the importance of stationary process or topographic effect, but also investigate the collective effects of the standing wave, cross-scale interaction, and subfilter eddy-eddy interaction on the filtered space-time scale from the perspective of triad interaction.

586 The discussions of scale separate filter, Leonard’s decomposition, and Germano identity
 587 help form a new paradigm of viewing the subgrid transport process with the hope
 588 of being aligned with numerical model practice as much as possible. We emphasize the
 589 complete eddy flux and LES framework need to be considered in the subgrid parameter-
 590 ization of coarse resolution or even non-eddy resolving ocean general circulation model.
 591 That is, besides the collective effect of subgrid eddy-eddy interaction represented by the
 592 Reynolds term, the Leonard and cross terms should also be parameterized to compen-
 593 sate for the missing standing wave effect and cross-scale interaction. In addition to the
 594 aforementioned points, the diagnostics in this paper are isoneutral, so the problem is sim-
 595 plified into 2D, and the neighboring sampling regression method is used to solve the un-
 596 nderdetermined problem of estimating the transport tensor or coefficient when using a sin-
 597 gular tracer. We also systematically investigate the performance of transport coefficients
 598 and transport tensors (mainly transport eigenvalues and eigenvectors) and the factors
 599 behind them under isotropy and anisotropy assumptions.

600 The main conclusions of this paper are as follows:

601 (1) From the stationary-transient decomposition, we found that the stationary ef-
 602 fect cannot be ignored for subfilter eddy transport and is primarily determined by the
 603 geographical distribution of topography. Topography not only directly engraves the sta-
 604 tionary structure of the PV flux field but also organizes the flow to generate transient
 605 adjustment processes near large-scale topography. As the spatial separation scale increases,
 606 the proportion of stationary contribution increases. This paper’s two sets of data are qual-
 607 itatively consistent in these characteristics.

608 (2) From Leonard’s decomposition, we found that it is necessary to consider the
 609 complete subgrid flux. Although there is a significant cancellation between the Leonard
 610 and Cross term, the sum of Leonard and Cross term is at least as critical as the Reynolds
 611 term. Their stationary parts dominate both terms. The Leonard term may be consid-
 612 ered as a large-scale standing wave effect, and the cross term represents the eddy-flow
 613 or small eddy versus large eddy interaction across the separation scale. They consist of
 614 several wave train structures and may reflect the system’s fingerprint shaped by the cur-
 615 rent geological, climate state, or model settings.

616 (3) The transport coefficient establishes the relationship between the length of the
 617 background PV gradient and the PV flux length. In its mathematical essence, the in-
 618 formation in different directions is mixed together, and the reconstructed meridional PV
 619 flux error is quite large. Instead, the anisotropic tensor greatly reduces the reconstruc-
 620 tion error because of its ability to distinguish the directionality of dynamic information,
 621 especially the anisotropy of the topographic anchoring effect.

622 (4) The sign combination of the transport eigenvalues of the symmetric tensor rep-
 623 represents its contribution to the large-scale PV enstrophy in the domain integral sense. All
 624 three cases occur in the SO, but in most regions the combination is (major +, minor -
 625), which means the dominance of the vortex filamentation process in the SO, and the pro-
 626 cess slightly dissipates large-scale enstrophy holistically. The relative difference between
 627 the two eigenvalues links to anisotropy, and the eddy transport process in the SO is highly
 628 anisotropic. The anisotropy at the pure source is slightly greater than that at the pure
 629 sink. The stationary standing wave effect and cross-scale interaction tend to enhance the
 630 anisotropy. In the region with stronger anisotropy, the dominant characteristic direction
 631 is easier to be perpendicular to the large-scale PV gradient, indicating that the PV bar-
 632 rier mechanism would significantly enhance the anisotropy of the eddy transport pro-
 633 cess.

634 As a preliminary work, this study only focuses on establishing the research frame-
 635 work, data with higher resolution, and larger research areas should be selected for more
 636 in-depth research in the future. In terms of data resolution, we try to balance between

637 reducing the amount of calculation and ensuring sufficient resolution to study the filter-
 638 ing scale phenomenon. On the one hand, the resolution of the current non-eddy resolv-
 639 ing or eddy-permitting ocean general circulation model can be less than 1° . According
 640 to the Germano identity, considering the implicit filter effect of resolution and sufficient
 641 buffer scale band, the data resolution used to approximate DNS needs to be at least $1/12^\circ$.
 642 In this sense, the results from our data and filter scale fail to directly provide quantita-
 643 tive suggestions for the eddy parameterization but only enlighten the possibility of a scheme
 644 more in line with the realistic oceanic eddy transport process, and attention should be
 645 paid to the qualitative characteristics diagnosed. On the other hand, using the highest
 646 resolution data nowadays (up to $1/50^\circ$ or even higher) as close to DNS as possible can
 647 allow systematic exploration of the scale dependence of stationary-transient decompo-
 648 sition, Leonard’s decomposition, and potential subgrid scheme in both spectral space and
 649 physical space, which will be a promising application of this framework. In addition, the
 650 temporal resolution and duration of the data in this paper only meet the minimum re-
 651 quirements. If climate research is carried out or submesoscale processes are considered,
 652 one should use long-time data or data with higher temporal resolution. The study area
 653 is limited to the SO and studying the other three ocean basins might lead to some new
 654 features.

655 In addition, some works (e.g., Haigh & Berloff, 2021; Haigh et al., 2021a, 2021b;
 656 Sun et al., 2021) used the divergent part of the eddy flux under the Helmholtz decom-
 657 position, because the net dynamic effect on the evolution of large-scale tracer field in equa-
 658 tion (2) is the eddy flux divergence. However, when the domain is bounded, the result
 659 of the rotation-divergence decomposition of the flux is not unique, complicating the prob-
 660 lem (Fox-Kemper et al., 2003; Bachman et al., 2015). Secondly, although some works,
 661 such as Maddison et al. (2015), have proposed some promising methods of implement-
 662 ing this decomposition, the definition of the boundary would be blurred after spatial coarse-
 663 graining (Buzdicotti et al., 2021), which makes it impossible to artificially specify the bound-
 664 ary conditions of rotational and divergent flux when solving the partial differential equa-
 665 tion under the Helmholtz decomposition (in fact, only the complete flux on the bound-
 666 ary can be known) and would affect the result of divergent flux. In practice, it may be
 667 a more natural choice to obtain the original flux first, and then directly remove any non-
 668 divergence part through the divergence operator (Fox-Kemper et al., 2003). Finally, tracer
 669 transport has a clear and concise physical meaning connected with parcel excursion the-
 670 ory (Taylor, 1922; Bachman et al., 2015). Therefore, our diagnostic framework only dis-
 671 cusses the original flux without the rotation-divergence decomposition.

672 To sum up, our framework should be regarded as a new tool or a new thinking paradigm
 673 for classifying, extracting, and integrating the information of complex eddy transport
 674 processes. It cannot directly specify the dynamic mechanism, so it must be combined
 675 with other theories to validate and explain the phenomenon. An example is the frame-
 676 work can reflect some characteristics of topographic effect but cannot directly describe
 677 the intermediate physical process or mechanism of how a specific type of topography ex-
 678 erts its influence. Therefore, further research on topographic effects based on our frame-
 679 work should be combined with well-designed idealized numerical experiments for our fu-
 680 ture work orientation.

681 Appendix A

682 Here we discuss the conceptual difference between the subfilter scale and subgrid-
 683 scale. In LES, Germano et al. (1991) and Germano (1992) proposed the so-called Ger-
 684 mano identity,

$$\mathbf{F}_{\text{sfs}} \equiv \overline{\overline{\mathbf{u}}^G \overline{c}^G}^F - \overline{\overline{\mathbf{u}}^F \overline{c}^F}^G \quad (\text{A1})$$

685 $-\overline{G}$ is an implicit filter with unknown expressions, such as the numerical grid discretiza-
 686 tion scheme or data resolution limit, and $-F$ is an explicit filter of a given specific form,

687 such as the boxcar filter used in this paper. The original variables should be the true fields
688 or direct numerical simulation (DNS).

689 In this study, these two datasets used are not from DNS, so the implicit filter is
690 the grid resolution limit of SOSE or LICOM. According to Germano identity, the subgrid-
691 scale refers to scales missed or poorly described in the dataset. Information in scales smaller
692 than grid scale is eliminated, and physical processes in a range of scales slightly larger
693 than the grid resolution would be underestimated or misrepresented. Based on the ex-
694 perience that numerical simulation requires at least five or six grid points to capture a
695 structure better, we assume that the ultimately influenced scale of an implicit filter would
696 reach a spatial scale six times its resolution, for example, 1° for SOSE and 0.6° for LI-
697 COM. On the scales larger than the ultimately influenced scale, we suppose they can re-
698 present the physical processes in a relatively sound manner. Therefore, the data used in
699 this paper are sufficient to study the part with a larger horizontal scale of the mesoscale
700 processes, not small eddies, in the SO.

701 As for the explicit filter in Germano identity, the boxcar filter is used in this pa-
702 per, which determines the so-called subfilter scale. Liu et al. (1994) systematically dis-
703 cusses the application of boxcar filter, Gaussian filter, and spectral truncation filter in
704 LES. He found that using a boxcar filter and Gaussian filter can achieve a high corre-
705 lation between the stress field predicted by LES and the observed stress field. Boxcar
706 filter is not a clean truncation in spectral space [Fig. 4 of Ciofalo (1994)]. When it is smaller
707 (greater) than the characteristic wavenumber (spatial scale) of the filter, the boxcar fil-
708 ter's Fourier spectrum, which can be deemed as spectral weights for fields under filter-
709 ing, rises from 0 to 1, namely, the process slightly larger than the filter scale would be
710 partially weakened, while the process much larger than the filter scale would be barely
711 changed; When it is greater (smaller) than the characteristic wavenumber (spatial scale)
712 of the filter, the spectral weight of boxcar filter oscillates up and down around the zero
713 axis and converges rapidly, that is, the process of the smaller scale is nearly eliminated.
714 In addition, the boxcar filter is equivalent to the mean value of all grid points in a given
715 box (the weight is only determined by grid area or volume), which makes the flux on the
716 box's boundary reflect the average change of the physical field inside the box, which is
717 similar to latitude-longitude grid discretization and finite volume method. Therefore, we
718 choose the boxcar filter for spatial coarse-graining.

719 From above, only when the scale of the selected explicit filter (the separation scale
720 of spatial coarse-graining) is sufficiently larger than the scale of the implicit resolution
721 filter the subfilter effect discussed be meaningful, and the data can be considered almost
722 as DNS. Otherwise, it would lose too much local and non-local triad interaction for the
723 subfilter scale, which might severely distort the microstructure of turbulence in the spec-
724 tral space near the filter scale, making it impossible to reach a practical conclusion. There-
725 fore, this paper focuses on the results under 2° boxcar filtering, which leaves a sufficient
726 buffer zone between the implicit filter scales of SOSE and LICOM. This allows the lo-
727 cal triad containing the subfilter scale wave vector that slightly smaller than the spatial
728 separation scale to be reliable. Still, the influence of the non-local triad containing the
729 smaller scale wave vector may be significantly underestimated.

730 Appendix B

731 Inspired by Kraichnan (1967); Gong et al. (1999); Vallis (2017); Zhou (2021), here
732 we will discuss three categories of triad interaction in spectral space under scale sepa-
733 ration of clear and unclear spectral truncation and reveal its relationship with Leonard's
734 decomposition.

735 The free evolving PV equation in spectral space is,

$$\frac{\partial}{\partial t} \hat{q}(\mathbf{k}) = \sum_{\mathbf{k}=\mathbf{m}+\mathbf{n}} N(\mathbf{k} | \mathbf{m}, \mathbf{n}) \quad (\text{B1})$$

$$q = \sum_{\mathbf{k}} \hat{q}(\mathbf{k}) e^{i\mathbf{k}\cdot\mathbf{x}} \quad (\text{B2})$$

$$N(\mathbf{k} | \mathbf{m}, \mathbf{n}) = a_i(\mathbf{k}) \hat{u}_i(\mathbf{m}) \hat{q}(\mathbf{n}) \quad (\text{B3})$$

736 N defines a single triad, i in Eq.B3 satisfies Einstein's summation convention, \hat{u}_i is the
 737 velocity component in the spectral space, and a_i is weights related to the wavenumber
 738 caused by the partial-differential operator. Due to the orthogonality of the basis func-
 739 tion, only the wave vectors \mathbf{m} and \mathbf{n} , which can form a triangle with \mathbf{k} , would affect the
 740 evolution of the specified PV spectrum $\hat{q}(\mathbf{k})$. Given a clear truncation scale \mathbf{k}_c in the spec-
 741 tral space, we can divide all wavenumbers in the whole spectral space into two cases: re-
 742 solved (or filtered) and subgrid (or subfilter) wavenumbers, namely

$$\mathbf{k} = \begin{cases} \mathbf{k}_r, & \text{if } |\mathbf{k}| \leq \mathbf{k}_c \\ \mathbf{k}_s, & \text{if } |\mathbf{k}| > \mathbf{k}_c \end{cases} \quad (\text{B4})$$

743 then the PV spectrum can be written as

$$\hat{q}(\mathbf{k}) = \begin{cases} \hat{q}_r(\mathbf{k}_r), & \text{if } |\mathbf{k}| \leq \mathbf{k}_c \\ \hat{q}_s(\mathbf{k}_s), & \text{if } |\mathbf{k}| > \mathbf{k}_c \end{cases} \quad (\text{B5})$$

$$q_r = \sum_{\mathbf{k}_r} \hat{q}_r(\mathbf{k}) e^{i\mathbf{k}\cdot\mathbf{x}} \quad (\text{B6})$$

$$q_s = \sum_{\mathbf{k}_s} \hat{q}_s(\mathbf{k}) e^{i\mathbf{k}\cdot\mathbf{x}} \quad (\text{B7})$$

744 Apply Eq.B4 - Eq.B7 to Eq.B1, we obtain the resolved (or filtered) scale PV spectrum
 745 equation,

$$\frac{\partial}{\partial t} \hat{q}_r(\mathbf{k}_r) = N_r(\mathbf{k}_r) + N_{crs}(\mathbf{k}_r) + N_s(\mathbf{k}_r) \quad (\text{B8})$$

$$N_r(\mathbf{k}_r) = \sum_{\mathbf{k}_r=\mathbf{m}_r+\mathbf{n}_r} N(\mathbf{k}_r | \mathbf{m}_r, \mathbf{n}_r) \quad (\text{B9})$$

$$N_{crs}(\mathbf{k}_r) = \sum_{\mathbf{k}_r=\mathbf{m}_r+\mathbf{n}_s} N(\mathbf{k}_r | \mathbf{m}_r, \mathbf{n}_s) + \sum_{\mathbf{k}_r=\mathbf{m}_s+\mathbf{n}_r} N(\mathbf{k}_r | \mathbf{m}_s, \mathbf{n}_r) \quad (\text{B10})$$

$$N_s(\mathbf{k}_r) = \sum_{\mathbf{k}_r=\mathbf{m}_s+\mathbf{n}_s} N(\mathbf{k}_r | \mathbf{m}_s, \mathbf{n}_s) \quad (\text{B11})$$

746 The subscript \mathbf{r} of this appendix means the quantity is in the resolved or filtered range,
 747 and the subscript \mathbf{s} for subgrid or subfilter range. The right side of Eq.B8 includes three
 748 categories of triad terms with different microstructures: N_r represents the collective ef-
 749 fect of two resolved wave vectors, namely \mathbf{m}_r and \mathbf{n}_r , on the PV spectrum of a given wavenum-
 750 ber \mathbf{k}_r at the resolved scale $\hat{q}_r(\mathbf{k}_r)$; N_{crs} represents the collective effect of two wave vec-
 751 tors from different ranges on $\hat{q}_r(\mathbf{k}_r)$; N_s represents the collective effect of two subgrid
 752 wave vectors \mathbf{m}_s and \mathbf{n}_s .

753 Next, we consider the case that the scale separation is not clear spectral trunca-
 754 tion, that is, the case of boxcar spatial coarse-graining adopted in this paper. Accord-
 755 ing to the convolution theorem, the large spatial scale field $[q]$ and spatial eddying field
 756 q^* can be expressed as

$$[q] = q_r = \sum_{\mathbf{k}} \hat{G}(\mathbf{k}) \hat{q}(\mathbf{k}) e^{i\mathbf{k}\cdot\mathbf{x}} \quad (\text{B12})$$

$$q^* = q_s = \sum_{\mathbf{k}} [1 - \hat{G}(\mathbf{k})] \hat{q}(\mathbf{k}) e^{i\mathbf{k}\cdot\mathbf{x}} \quad (\text{B13})$$

757 The separation scale now is not certain, so we generalize the separation scale into a sep-
 758 aration scale interval,

$$\widetilde{\mathbf{k}}_{\mathbf{c}} \in [\mathbf{k}_{\mathbf{c}}^-, \mathbf{k}_{\mathbf{c}}^+] \quad (\text{B14})$$

759 $\mathbf{k}_{\mathbf{c}}^-$ is the lower wavenumber bound with a significant magnitude of the subfilter quan-
 760 tity, and $\mathbf{k}_{\mathbf{c}}^+$ is the upper wave number bound with a significant magnitude of the fil-
 761 tered field. The separation scale interval is the cross wave number interval of the two.
 762 In this way, the generalized resolved wave number $\widetilde{\mathbf{k}}_r$ and subgrid wave number $\widetilde{\mathbf{k}}_s$

$$\widetilde{\mathbf{k}}_r \in (0, \mathbf{k}_{\mathbf{c}}^+] \quad (\text{B15})$$

$$\widetilde{\mathbf{k}}_s \in [\mathbf{k}_{\mathbf{c}}^-, \infty) \quad (\text{B16})$$

763 generalize the spectrum of a specified quantity, for example for generalized PV spectrum

$$\hat{\tilde{q}}(\mathbf{k}) \equiv \begin{cases} \hat{\tilde{q}}_r(\widetilde{\mathbf{k}}_r) \equiv \hat{G}(\widetilde{\mathbf{k}}_r) \hat{q}(\widetilde{\mathbf{k}}_r), & \text{if } \mathbf{k} \in \text{filtered sector} \\ \hat{\tilde{q}}_s(\widetilde{\mathbf{k}}_s) \equiv [1 - \hat{G}(\widetilde{\mathbf{k}}_s)] \hat{q}(\widetilde{\mathbf{k}}_s), & \text{if } \mathbf{k} \in \text{subfiltered sector} \end{cases} \quad (\text{B17})$$

764 the generalized form of resolved (or filtered) scale PV spectrum equation is

$$\frac{\partial}{\partial t} \hat{\tilde{q}}_r(\widetilde{\mathbf{k}}_r) = \widetilde{N}_r(\widetilde{\mathbf{k}}_r) + \widetilde{N}_{crs}(\widetilde{\mathbf{k}}_r) + \widetilde{N}_s(\widetilde{\mathbf{k}}_r) \quad (\text{B18})$$

$$\widetilde{N}_r(\widetilde{\mathbf{k}}_r) = \sum_{\widetilde{\mathbf{k}}_r = \widetilde{\mathbf{m}}_r + \widetilde{\mathbf{n}}_r} \widetilde{N}(\widetilde{\mathbf{k}}_r | \widetilde{\mathbf{m}}_r, \widetilde{\mathbf{n}}_r) \quad (\text{B19})$$

$$\widetilde{N}_{crs}(\widetilde{\mathbf{k}}_r) = \sum_{\widetilde{\mathbf{k}}_r = \widetilde{\mathbf{m}}_r + \widetilde{\mathbf{n}}_s} \widetilde{N}(\widetilde{\mathbf{k}}_r | \widetilde{\mathbf{m}}_r, \widetilde{\mathbf{n}}_s) + \sum_{\widetilde{\mathbf{k}}_r = \widetilde{\mathbf{m}}_s + \widetilde{\mathbf{n}}_r} \widetilde{N}(\widetilde{\mathbf{k}}_r | \widetilde{\mathbf{m}}_s, \widetilde{\mathbf{n}}_r) \quad (\text{B20})$$

$$\widetilde{N}_s(\widetilde{\mathbf{k}}_r) = \sum_{\widetilde{\mathbf{k}}_r = \widetilde{\mathbf{m}}_s + \widetilde{\mathbf{n}}_s} \widetilde{N}(\widetilde{\mathbf{k}}_r | \widetilde{\mathbf{m}}_s, \widetilde{\mathbf{n}}_s) \quad (\text{B21})$$

$$\widetilde{N}(\widetilde{\mathbf{k}} | \widetilde{\mathbf{m}}, \widetilde{\mathbf{n}}) = a_i(\widetilde{\mathbf{k}}) \hat{\mathbf{u}}_i(\widetilde{\mathbf{m}}) \hat{q}(\widetilde{\mathbf{n}}) \quad (\text{B22})$$

765 consistent with the form of Eq.B8 - Eq.B11 under clear spectrum truncation, there are
 766 three kinds of triad interaction terms with different microstructures. The difference is
 767 that their wave vectors have different number (0, 1, and 2) of subfilter quantities par-
 768 ticipating in the triad interaction. In Leonard's decomposition in this paper, $\widetilde{N}_r(\widetilde{\mathbf{k}}_r)$
 769 corresponds to the sum of the Leonard term and large-scale transport term, $\widetilde{N}_{crs}(\widetilde{\mathbf{k}}_r)$
 770 corresponds to the cross term, $\widetilde{N}_s(\widetilde{\mathbf{k}}_r)$ corresponds to the Reynolds term.

Appendix C

A brief example is given to illustrate the mass- or volume-weighted interpolation method: if the target neutral plane is 36.8kg/m^3 , for each water column, find the depths of neutral planes of 36.75 and 36.85kg/m^3 , and take the weighted average of the velocities on all z -coordinate levels between the two depths (the weight depends on the proportion of each z -coordinate level in the total depth difference, i.e., mass or volume weight) as the velocity on the 36.8kg/m^3 neutral plane.

Another example illustrates how the least square regression of neighboring samples can solve the underdetermined problem when calculating the transport coefficient and tensor. For a given center point, say (120°E , 45°S), take the eddy flux and large-scale PV gradient on the neighboring $(2p+1)^2$ grid points as samples. Then least-square regress these $(2p+1)^2$ pairs of data to estimate quasi-localized transport tensor or coefficient at the central point (120°E , 45°S). This method has the advantages of convenience and a small amount of calculation and allows to handle the observed data or numerical results without enough numbers of passive tracers. In our method, the size of sampling area p would affect the reconstruction accuracy of the eddy flux. The smaller p is, the more localized the samples are, and the closer the reconstructed flux to the actual value. The smaller the ratio of sampling area size p to filter size ir , the smoother the physical field that makes the slowly varying hypothesis valid, and the higher the reconstruction accuracy. However, the influence of p/ir is not as dramatic as merely decreasing p . What we show in this paper is 9-point sampling with $p = 1$.

Acknowledgments

This study was supported by the National Natural Science Foundation of China (Grants 41931183, 41976026, and 41931182), the National Key RD Program for Developing Basic Sciences (2018YFA0605703), and the Strategic Priority Research Program of the Chinese Academy of Sciences (Grant No. XDB42010404). HLL and PFL also acknowledge the technical support from the National Key Scientific and Technological Infrastructure project "Earth System Science Numerical Simulator Facility" (EarthLab). Southern Ocean State Estimate (SOSE) data can be found in <https://climatedataguide.ucar.edu/climate-data/southern-ocean-state-estimate-bose>. The data and code used in the figures can be obtained online (<http://data.lasg.ac.cn/lhl/data-hybrid-framework/>).

References

- Abernathey, R., & Cessi, P. (2014). Topographic enhancement of eddy efficiency in baroclinic equilibration. *Journal of Physical Oceanography*, *44*(8), 2107-2126. doi: 10.1175/JPO-D-14-0014.1
- Aluie, H., Hecht, M., & Vallis, G. (2018). Mapping the energy cascade in the north atlantic ocean: The coarse-graining approach. *Journal of Physical Oceanography*, *48*(2), 225-244. doi: 10.1175/JPO-D-17-0100.1
- Anderson, B., & Domaradzki, J. (2012). A subgrid-scale model for large-eddy simulation based on the physics of interscale energy transfer in turbulence. *Physics of Fluids*, *24*(6), 99-164. doi: 10.1063/1.4729618
- Bachman, S. (2019). The gm+e closure: A framework for coupling backscatter with the gent and mcwilliams parameterization. *Ocean Modelling*, *136*, 85-106. doi: <https://doi.org/10.1016/j.ocemod.2019.02.006>
- Bachman, S., & Fox-Kemper, B. (2013). Eddy parameterization challenge suite i: Eady spindown. *Ocean Modelling*, *64*(Complete), 12-28. doi: <https://doi.org/10.1016/j.ocemod.2012.12.003>
- Bachman, S., Fox-Kemper, B., & Bryan, F. (2015). A tracer-based inversion method for diagnosing eddy-induced diffusivity and advection. *Ocean Modelling*, *86*, 1-14. doi: <https://doi.org/10.1016/j.ocemod.2014.11.006>

- 821 Bachman, S., Fox-Kemper, B., & Bryan, F. (2020). A diagnosis of anisotropic eddy
822 diffusion from a high-resolution global ocean model. *Journal of Advances in*
823 *Modeling Earth Systems*, 12(2), e2019MS001904. doi: [https://doi.org/10.1029/](https://doi.org/10.1029/2019MS001904)
824 2019MS001904
- 825 Berloff, P. (2005). Random-forcing model of the mesoscale oceanic eddies. *Journal of*
826 *Fluid Mechanics*, 529, 71-95. doi: 10.1017/S0022112005003393
- 827 Bischoff, T., & Thompson, A. (2014). Configuration of a southern ocean storm
828 track. *Journal of Physical Oceanography*, 44(12), 3072-3078. doi: 10.1175/JPO
829 -D-14-0062.1
- 830 Buzziotti, M., Storer, B., Griffies, S., & Aluie, H. (2021). A coarse-grained decom-
831 position of surface geostrophic kinetic energy in the global ocean. *Earth and*
832 *Space Science Open Archive*, 58. doi: 10.1002/essoar.10507290.1
- 833 Cessi, P. (2007). An energy-constrained parameterization of eddy buoy-
834 ancy flux. *Journal of Physical Oceanography*, 38(8), 1807-1819. doi:
835 10.1175/2007JPO3812.1
- 836 Chapman, C., Hogg, A., Kiss, A., & Rintoul, S. (2015, 02). The dynamics
837 of southern ocean storm tracks. *Journal of Physical Oceanography*, 45,
838 150209131807009. doi: 10.1175/JPO-D-14-0075.1
- 839 Ciofalo, M. (1994). *Large-eddy simulation: A critical survey of models and applica-*
840 *tions*. Academic Press.
- 841 Clark, R. (1977). Evaluation of subgrid-scale turbulence models using a fully simu-
842 lated turbulent flow.
- 843 Clark, R., Ferziger, J., & Reynolds, W. (1979). Evaluation of subgrid-scale mod-
844 els using an accurately simulated turbulent flow. *Jour Fluid Mech*, 91(01), 1-
845 16. doi: 10.1017/S002211207900001X
- 846 Dukowicz, J., & Smith, R. (1997). Stochastic theory of compressible turbulent fluid
847 transport. *Physics of Fluids*, 9(11), 3523-3529. doi: 10.1063/1.869460
- 848 Eden, C., & Greatbatch, R. (2008). Towards a mesoscale eddy closure. *Ocean Mod-*
849 *elling*, 20(3), 223-239. doi: 10.1016/j.ocemod.2007.09.002
- 850 Ferrari, R., & Nikurashin, M. (2010). Suppression of eddy diffusivity across jets in
851 the southern ocean. *Journal of Physical Oceanography*, 40(7), 1501-1519. doi:
852 10.1175/2010JPO4278.1
- 853 Fox-Kemper, B., Ferrari, R., & Pedlosky, J. (2003, 02). On the indeterminacy of
854 rotational and divergent eddy fluxes. *Journal of Physical Oceanography - J*
855 *PHYS OCEANOGR*, 33, 478-483. doi: 10.1175/1520-0485(2003)033<0478:
856 OTIORA>2.0.CO;2
- 857 Fox-Kemper, B., Lumpkin, R., & Bryan, F. (2013). *Lateral transport in the ocean*
858 *interior*. International Geophysics. doi: [https://doi.org/10.1016/B978-0-12-](https://doi.org/10.1016/B978-0-12-391851-2.00008-8)
859 -391851-2.00008-8
- 860 Fox-Kemper, B., & Menemenlis, D. (2008). Can large eddy simulation techniques
861 improve mesoscale rich ocean models? *Washington DC American Geophysical*
862 *Union Geophysical Monograph Series*, 177, 319-337. doi: 10.1029/177GM19
- 863 Galmarini, S., Michelutti, F., & Thunis, P. (2000). Estimating the contribution of
864 leonard and cross terms to the subfilter scale from atmospheric measurements.
865 *J. Atmos. Sci.*. doi: 10.1175/1520-0469(2000)057<2968:etcola>2.0.co;2
- 866 Garabato, A., Ferrari, R., & Polzin, K. (2011). Eddy stirring in the southern ocean.
867 *Journal of Geophysical Research*. doi: 10.1029/2010jc006818
- 868 Gent, & McWilliams, J. (1990). Isopycnal mixing in ocean circulation models. *Jour-*
869 *nal of Physical Oceanography*, 20(1), 150-155. doi: 10.1175/1520-0485(1990)
870 0202.0.CO;2
- 871 Gent, P., McDougall, T., & McWilliams, J. (1995). Parameterizing eddy-induced
872 tracer transports in ocean circulation models. *J.phys.oceanogr*, 25(4), 463-474.
873 doi: 10.1175/1520-0485(1995)0252.0.CO;2
- 874 Germano, M. (1992). Turbulence-the filtering approach. *Journal of Fluid Mechanics*,
875 238(-1). doi: 10.1017/S0022112092001733

- 876 Germano, M., Piomelli, U., Moin, P., & Cabot, W. (1991). A dynamic subgrid-scale
877 eddy viscosity model. *Physics of Fluids*, *3*(3), 1760-1765. doi: [https://doi.org/](https://doi.org/10.1063/1.857955)
878 [10.1063/1.857955](https://doi.org/10.1063/1.857955)
- 879 Gong, H., Chen, S., & He, G. (1999). An analysis of subgrid-resolved scale inter-
880 actions with use of results from direct numerical simulations. *Acta Mechanica*
881 *Sinica*. doi: [10.1007/BF02485875](https://doi.org/10.1007/BF02485875)
- 882 Griffies, S. (1998). The gent–mcwilliams skew flux. *J.phys.oceanogr*, *28*(5), 831-841.
883 doi: [10.1175/1520-0485\(1998\)0282.0.CO;2](https://doi.org/10.1175/1520-0485(1998)0282.0.CO;2)
- 884 Griffies, S., Gnanadesikan, A., Pacanowski, R., Larichev, V., & Smith, R. (1998).
885 Isonutral diffusion in a z-coordinate ocean model. *J.phys.oceanogr*, *28*(5),
886 805-830. doi: [10.1175/1520-0485\(1998\)0282.0.CO;2](https://doi.org/10.1175/1520-0485(1998)0282.0.CO;2)
- 887 Groeskamp, S., Lacasce, J., Mcdougall, T., & Rogé, M. (2020). Full-depth global
888 estimates of ocean mesoscale eddy mixing from observations and theory. *Geo-*
889 *physical Research Letters*, *47*. doi: <https://doi.org/10.1029/2020GL089425>
- 890 Haigh, M., & Berloff, P. (2021). On co-existing diffusive and anti-diffusive tracer
891 transport by oceanic mesoscale eddies. *Ocean Modelling*, *168*, 101909-. doi:
892 <https://doi.org/10.1016/j.ocemod.2021.101909>
- 893 Haigh, M., Sun, L., Mcwilliams, J., & Berloff, P. (2021a). On eddy transport in the
894 ocean. part ii: The advection tensor. *Ocean Modelling*, *165*. doi: [10.1016/j](https://doi.org/10.1016/j.ocemod.2021.101845)
895 [.ocemod.2021.101845](https://doi.org/10.1016/j.ocemod.2021.101845)
- 896 Haigh, M., Sun, L., Mcwilliams, J., & Berloff, P. (2021b). On eddy transport in the
897 ocean. part i: The diffusion tensor. *Ocean Modelling*, *164*(1), 101831. doi: [10](https://doi.org/10.1016/j.ocemod.2021.101831)
898 [.1016/j.ocemod.2021.101831](https://doi.org/10.1016/j.ocemod.2021.101831)
- 899 Haigh, M., Sun, L., Shevchenko, I., & Berloff, P. (2020). Tracer-based estimates of
900 eddy-induced diffusivities. *Deep Sea Research Part I Oceanographic Research*
901 *Papers*, *160*, 103264. doi: <https://doi.org/10.1016/j.dsr.2020.103264>
- 902 Hallberg, R. (2013). Using a resolution function to regulate parameterizations of
903 oceanic mesoscale eddy effects. *Ocean Modelling*, *72*(Complete), 92–103. doi:
904 <https://doi.org/10.1016/j.ocemod.2013.08.007>
- 905 Hewitt, H., Roberts, M., Mathiot, P., Biastoch, A., & Zhang, Q. (2020). Resolving
906 and parameterising the ocean mesoscale in earth system models. *Current Cli-*
907 *mate Change Reports*. doi: [10.1007/s40641-020-00164-w](https://doi.org/10.1007/s40641-020-00164-w)
- 908 Kamenkovich, I., Berloff, P., Haigh, M., Sun, L., & Lu, Y. (2021). Complexity of
909 mesoscale eddy diffusivity in the ocean. *Geophysical Research Letters*, *48*(5),
910 e2020GL091719. doi: <https://doi.org/10.1029/2020GL091719>
- 911 Khani, S., Jansen, M., & Adcroft, A. (2019). Diagnosing subgrid mesoscale eddy
912 fluxes with and without topography. *Journal of Advances in Modeling Earth*
913 *Systems*, *11*(12), 3995-4015. doi: <https://doi.org/10.1029/2019MS001721>
- 914 Kraichnan, R. H. (1967). Inertial ranges in two-dimensional turbulence. *Physics of*
915 *Fluids*, *10*. doi: [10.1063/1.1762301](https://doi.org/10.1063/1.1762301)
- 916 Ledwell, J., Watson, A., & Law, C. (1998). Mixing of a tracer in the pycnocline.
917 *Journal of Geophysical Research Oceans*, *103*(C10), 21499-21529. doi: [10.1029/](https://doi.org/10.1029/98JC01738)
918 [98JC01738](https://doi.org/10.1029/98JC01738)
- 919 Leonard, A. (1974). Energy cascade in large-eddy simulations of turbulent fluid
920 flows. In *Turbulent diffusion in environmental pollution*.
- 921 Liu, S., Meneveau, C., & Katz, J. (1994). On the properties of similarity subgrid-
922 scale models as deduced from measurements in a turbulent jet. *J Fluid Mech*.
923 doi: [10.1017/s0022112094002296](https://doi.org/10.1017/s0022112094002296)
- 924 Lu, J., Wang, F., Liu, H., & Lin, P. (2016). Stationary mesoscale eddies, upgradient
925 eddy fluxes, and the anisotropy of eddy diffusivity. *Geophysical Research Let-*
926 *ters*, *43*(2), 743-751. doi: <https://doi.org/10.1002/2015GL067384>
- 927 MacCready, P., & Rhines, P. (2001). Meridional transport across a zonal channel:
928 Topographic localization. *Journal of Physical Oceanography*, *31*(6), 1427-1439.
929 doi: [10.1175/1520-0485\(2001\)0312.0.CO;2](https://doi.org/10.1175/1520-0485(2001)0312.0.CO;2)
- 930 Maddison, J., Marshall, D., & Shipton, J. (2015). On the dynamical influence of

- 931 ocean eddy potential vorticity fluxes. *Ocean Modelling*, 92. doi: 10.1016/j.
932 .ocemod.2015.06.003
- 933 Mak, J., Marshall, D., Maddison, J., & Bachman, S. (2017). Emergent eddy saturation
934 from an energy constrained eddy parameterisation.
935 doi: <https://doi.org/10.1016/j.ocemod.2017.02.007>
- 936 Marshall, D., Maddison, J., & Berloff, P. (2012). A framework for parameterizing
937 eddy potential vorticity fluxes. *Journal of Physical Oceanography*, 42(4), 539-
938 557. doi: 10.1175/JPO-D-11-048.1
- 939 Marshall, D., Williams, R., & Lee, M. (1999). The relation between eddy-induced
940 transport and isopycnic gradients of potential vorticity. *J.phys.oceanogr*,
941 29(7), 1571-1578. doi: [doi:http://dx.doi.org/10.1175/1520-0485\(1999\)029<1571:](http://dx.doi.org/10.1175/1520-0485(1999)029<1571:TRBEIT>2.0)
942 [TRBEIT](http://dx.doi.org/10.1175/1520-0485(1999)029<1571:TRBEIT>2.0)2.0
- 943 Mazloff, M., Heimbach, P., & Wunsch, C. (2010). An eddy-permitting southern
944 ocean state estimate. *Journal of Physical Oceanography*, 40(5), 880-899. doi:
945 10.1175/2009JPO4236.1
- 946 McDougall, T. (1987). Neutral surfaces. *Journal of Physical Oceanography*, 17(17),
947 1950-1964. doi: 10.1175/1520-0485(1987)017<1546:CISSA>2.0.CO;2
- 948 McDougall, T., & McIntosh, P. (1996). The temporal-residual-mean velocity. part i:
949 Derivation and the scalar conservation equations. *Journal of Physical Oceanog-*
950 *raphy*, 26(12), 2653-2665. doi: 10.1175/1520-0485(1996)026<2653:TRMEV>2.0.CO;2
- 951 McDougall, T., & McIntosh, P. (2001). The temporal-residual-mean velocity. part
952 ii: Isopycnal interpretation and the tracer and momentum equations. *Journal*
953 *of Physical Oceanography*, 31(5), 1222-1246. doi: 10.1175/1520-0485(2001)031<1222:TRMEV>2.0.CO;2
- 954 .0.CO;2
- 955 Nakamura, N. (2001). A new look at eddy diffusivity as a mixing diagnostic. *Journal*
956 *of the Atmospheric Sciences*, 58(24), 3685-3701. doi: 10.1175/1520-0469(2001)
957 058<3685:anlaed>2.0.co;2
- 958 Radko, T., & Kamenkovich, I. (2017). On the topographic modulation of large-scale
959 eddy flows. *Journal of Physical Oceanography*, 47(9), 2157-2172. doi: 10
960 .1175/JPO-D-17-0024.1
- 961 Redi, M. (1982). Oceanic isopycnal mixing by coordinate rotation. *Journal of Phys-*
962 *ical Oceanography*, 12(10), 1154-1158. doi: 10.1175/1520-0485(1982)012<1154:ICMR>2.0.CO;2
- 963 2
- 964 Rintoul, S. R., Hughes, C. W., & Olbers, D. J. (2001). The antarctic circumpolar
965 current system. *Ocean Circulation Climate*(01), 271-302, XXIX-XXXVI. doi:
966 10.1016/S0074-6142(01)80124-8
- 967 Rypina, I., Kamenkovich, I., Berloff, P., & Pratt, L. J. (2012). Eddy-induced particle
968 dispersion in the near-surface north atlantic. *Chaos An Interdisciplinary Jour-*
969 *nal of Nonlinear Science*, 42(12), 2206-2228. doi: 10.1063/1.4927424
- 970 Smith, R., & Gent, P. (2004). Anisotropic gent-mcwilliams parameterization for
971 ocean models. *Journal of Physical Oceanography*, 34(11), 2541. doi: 10.1175/
972 JPO2613.1
- 973 Smith, S. (2005). Tracer transport along and across coherent jets in two-dimensional
974 turbulent flow. *Journal of Fluid Mechanics*, 544(-1), 133-142. doi: 10.1017/
975 S0022112005006750
- 976 Speziale, C. (1985). Galilean invariance of subgrid-scale stress models in the large-
977 eddy simulation of turbulence. *Journal of Fluid Mechanics*, 156(156), 55-62.
978 doi: 10.1017/S0022112085001987
- 979 Srinivasan, K., & Young, W. (2014). Reynolds stress and eddy diffusivity of -plane
980 shear flows. *Journal of the Atmospheric Sciences*, 71(6), 2169 - 2185. doi: 10
981 .1175/JAS-D-13-0246.1
- 982 Stanley. (2019). Neutral surface topology. *Ocean Modelling*. doi: 10.1016/j.ocemod
983 .2019.01.008
- 984 Stanley, Z., Bachman, S., & Grooms, I. (2020). Vertical structure of ocean mesoscale
985 eddies with implications for parameterizations of tracer transport. *Journal*

- 986 *of Advances in Modeling Earth Systems*, 12. doi: [https://doi.org/10.1029/](https://doi.org/10.1029/2020MS002151)
987 2020MS002151
- 988 Sun, L., Haigh, M., Shevchenko, I., Berloff, P., & Kamenkovich, I. (2021, 08). On
989 non-uniqueness of the mesoscale eddy diffusivity. *Journal of Fluid Mechanics*,
990 920. doi: 10.1017/jfm.2021.472
- 991 Taylor, G. (1922). Diffusion by continuous movements. *Proceedings of the London*
992 *Mathematical Society*, s2-20(1). doi: 10.1112/plms/s2-20.1.196
- 993 Thompson, A., & Garabato, A. (2014). Equilibration of the antarctic circumpolar
994 current by standing meanders. *Journal of Physical Oceanography*, 44(7), 1811
995 - 1828. doi: 10.1175/JPO-D-13-0163.1
- 996 Thompson, A., & Sallée, J. (2012). Jets and topography: Jet transitions and the
997 impact on transport in the antarctic circumpolar current. *Journal of Physical*
998 *Oceanography*, 42(6), 956-972. doi: 10.1175/JPO-D-11-0135.1
- 999 Thompson, A. F. (2010). Jet formation and evolution in baroclinic turbulence with
1000 simple topography. *J.phys.oceanogr*, 40(2), 257-278. doi: [http://dx.doi.org/10](http://dx.doi.org/10.1175/2009JPO4218.1)
1001 [.1175/2009JPO4218.1](http://dx.doi.org/10.1175/2009JPO4218.1)
- 1002 Treguier, A., Held, I., & Larichev, V. (1997). Parameterization of quasigeostrophic
1003 eddies in primitive equation ocean models. *J.phys.oceanogr*, 27(4), 567-580.
1004 doi: 10.1175/1520-0485(1997)0272.0.CO;2
- 1005 Treguier, A., & McWilliams, J. (1990). Topographic influences on wind-driven, strat-
1006 ified flow in a -plane channel: An idealized model of the antarctic circumpolar
1007 current. *J. Phys. Ocean.*, 20, 324-343. doi: 10.1175/1520-0485(1990)020<0321:
1008 T1OWDS>2.0.CO;2
- 1009 Vallis, G. (2017). *Atmospheric and oceanic fluid dynamics*.
- 1010 Visbeck, M., Marshall, J., Haine, T., & Spall, M. (1997). Specification of eddy trans-
1011 fer coefficients in coarse-resolution ocean circulation models. *Journal of Physi-*
1012 *cal Oceanography*, 27(3), 381-402. doi: 10.1175/1520-0485(1997)0272.0.CO;2
- 1013 Waterman, S., & Lilly, J. M. (2015, April). Geometric Decomposition of Eddy Feed-
1014 backs in Barotropic Systems. *Journal of Physical Oceanography*, 45(4), 1009-
1015 1024. doi: 10.1175/JPO-D-14-0177.1
- 1016 Wei, H., & Wang, Y. (2021). Full-depth scalings for isopycnal eddy mixing across
1017 continental slopes under upwelling-favorable winds. *Journal of Advances in*
1018 *Modeling Earth Systems*, 13. doi: 10.1029/2021MS002498
- 1019 Williams, Richard, G., Wilson, Chris, Hughes, ... W. (2007). Ocean and atmo-
1020 sphere storm tracks: The role of eddy vorticity forcing. *J. Phys. Oceanogr*. doi:
1021 [10.1175/jpo3120.1](https://doi.org/10.1175/jpo3120.1)
- 1022 Young, W., Rhines, P., & Garrett, C. (1982). Shear-flow dispersion, internal waves
1023 and horizontal mixing in the ocean. *Journal of Physical Oceanography*, 12(6),
1024 515-527.
- 1025 Youngs, M., Thompson, A., Lazar, A., & Richards, K. (2017). Acc meanders, en-
1026 ergy transfer, and mixed barotropic-baroclinic instability. *Journal of Physical*
1027 *Oceanography*, 47(6), 1291-1305. doi: 10.1175/JPO-D-16-0160.1
- 1028 Yu, Y. Q., Liu, H. L., & Lin, P. F. (2012). A quasi-global 1/10° eddy-resolving
1029 ocean general circulation model and its preliminary results. *Chinese Science*
1030 *Bulletin*. doi: 10.1007/s11434-012-5234-8
- 1031 Zhai, X., Johnson, H., & Marshall, D. (2010, 08). Significant sink of ocean-eddy en-
1032 ergy near western boundaries. *Nature Geoscience*, 3. doi: 10.1038/ngeo943
- 1033 Zhou, Y. (2021). Turbulence theories and statistical closure approaches. *Physics Re-*
1034 *ports*, 935(Suppl. 1). doi: 10.1016/j.physrep.2021.07.001

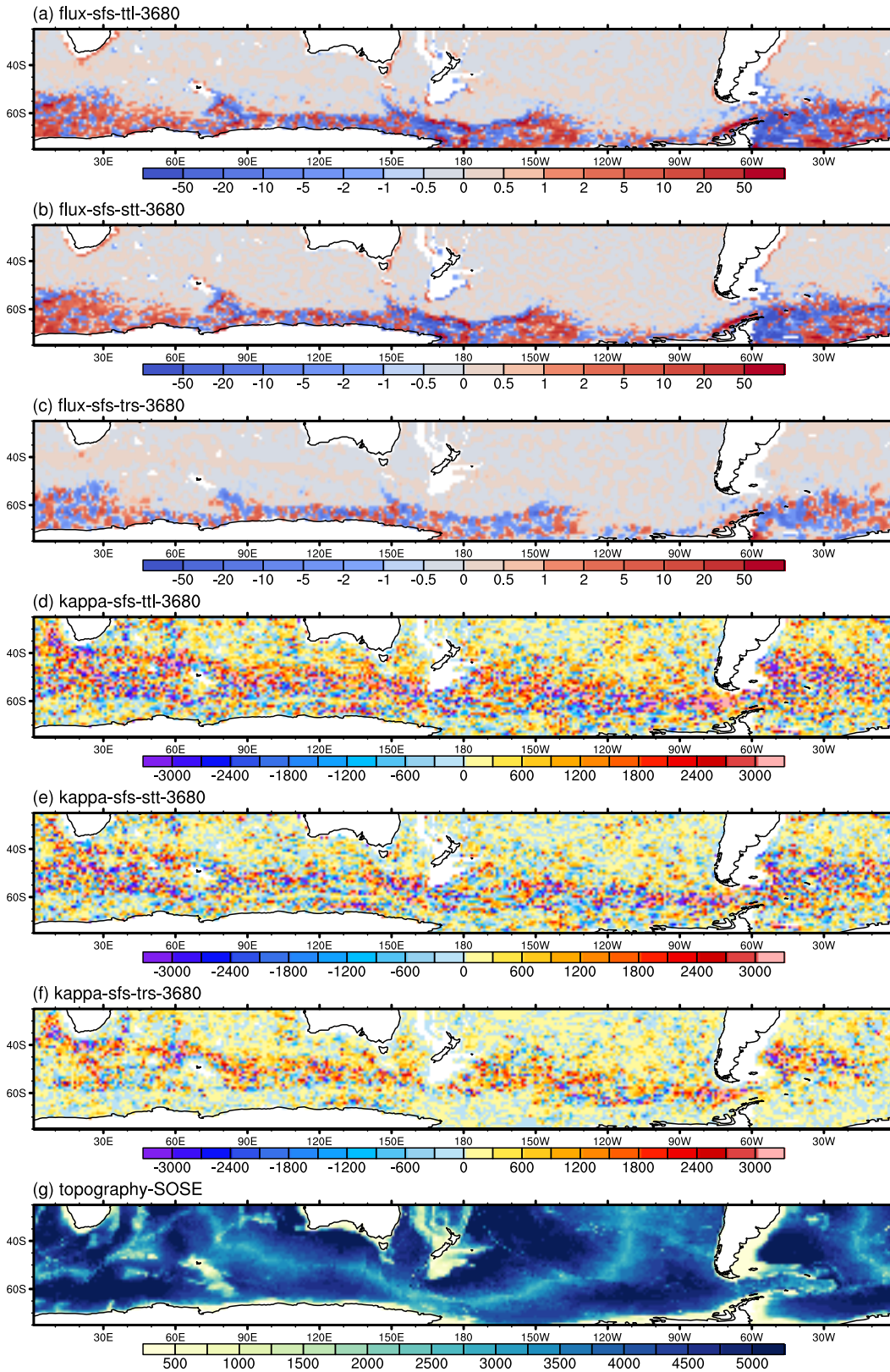


Figure C1. (a) total, (b) stationary, and (c) transient meridional subfilter PV flux, unit: 10^{-13} s^{-2} , (d) total, (e) stationary, and (f) transient isotropic subfilter transport coefficient, unit m^2/s , on the topobaric surface of 36.8 kg/m^3 , using 2° boxcar filter for SOSE, (g) large-scale topography (filtered by 2° boxcar filter) of SOSE, unit: m

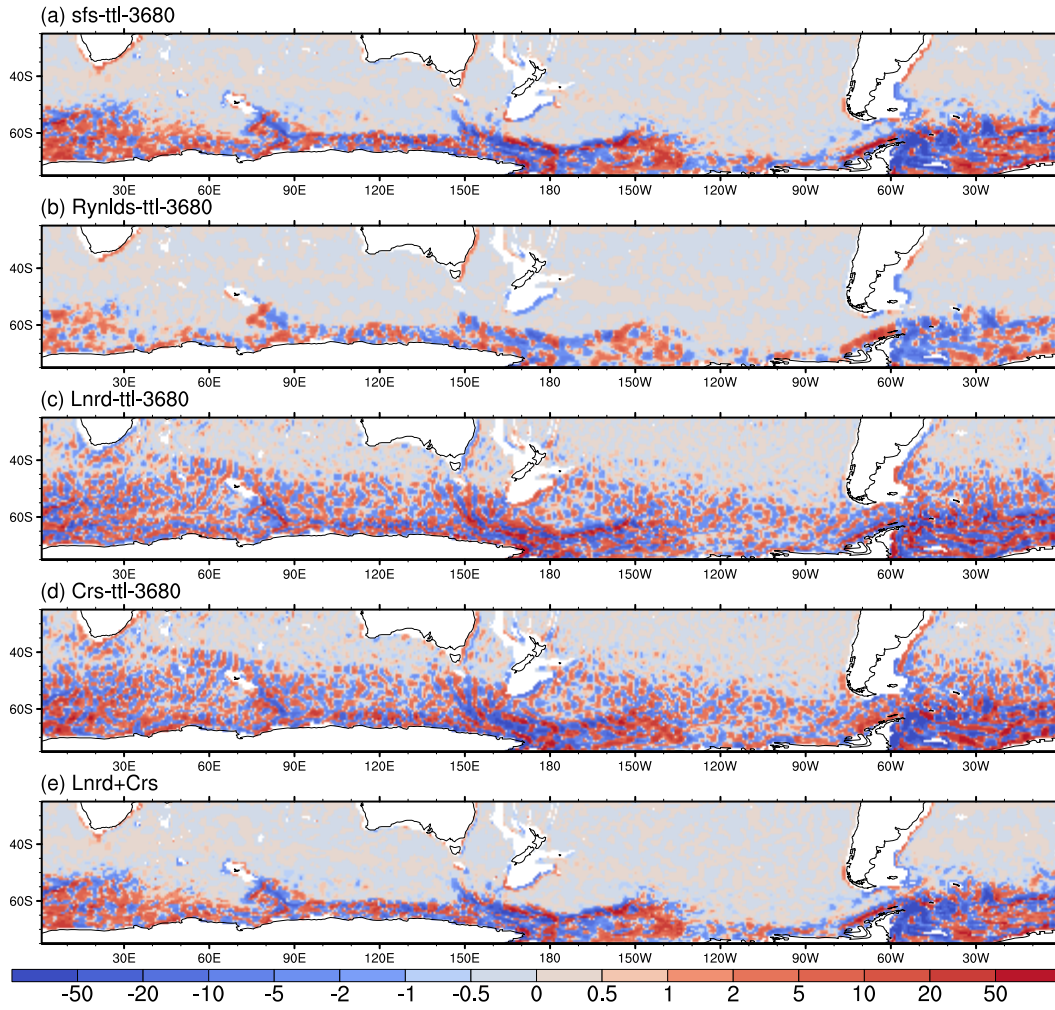


Figure C2. The total meridional subfilter PV flux of (a) complete subfilter, (b) Reynolds term, (c) Leonard term, (d) Cross term and (e) Leonard plus Cross term, unit: $1e-13$ S-2, on the topobaric surface of $36.8kg/m^3$, using 2° boxcar filter for SOSE

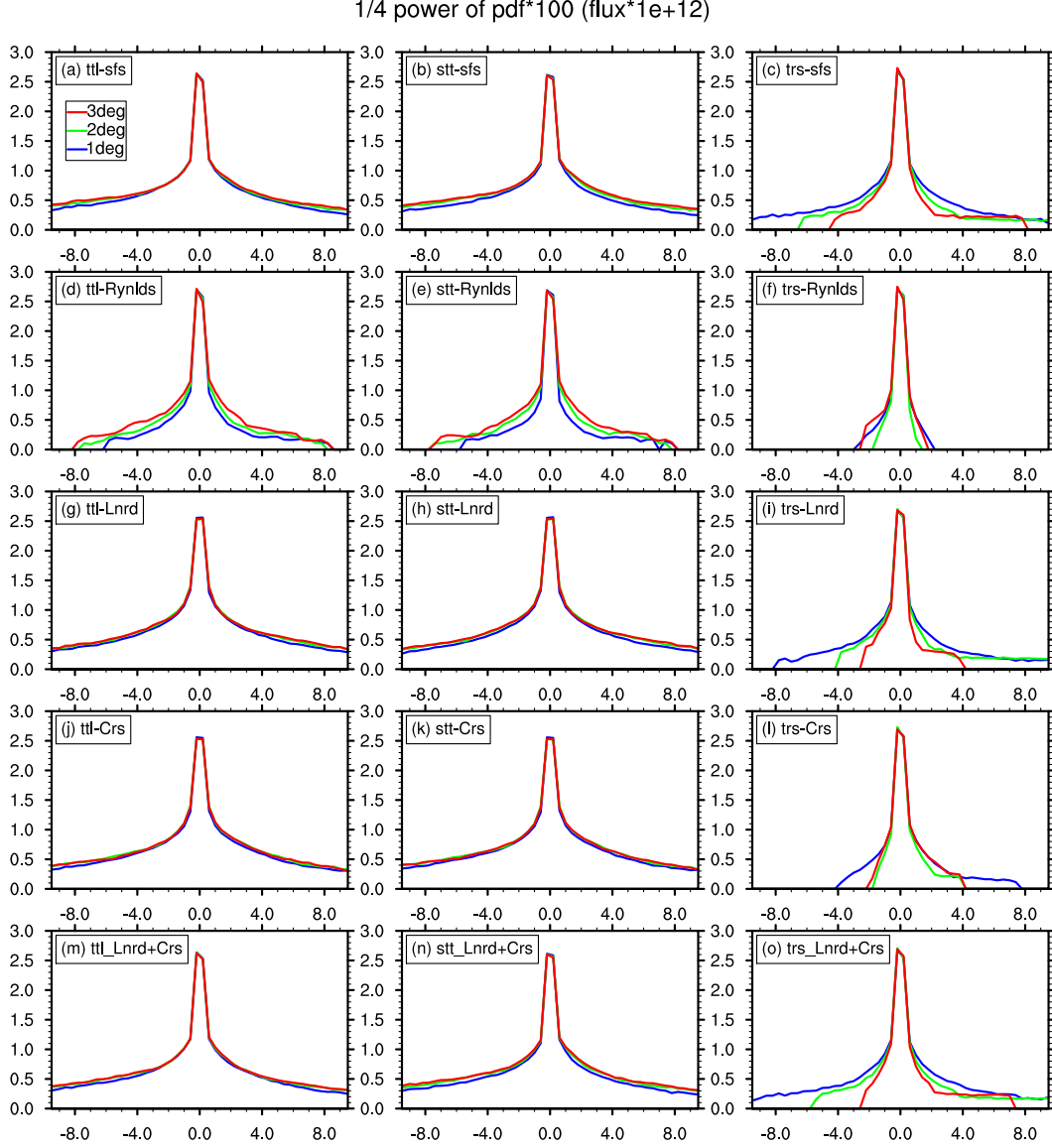


Figure C3. 1/4 power of the PDF of the meridional subfilter PV flux ($10^{-12} s^{-2}$) of SOSE, this scaling is for the convenience of drawing. The three columns from left to right are the total, stationary and transient parts, respectively. The five rows from top to bottom are the results of subfilter, Reynolds term, Leonard term, Cross term and the sum of Leonard and Cross term, respectively. blue, green, and red line for 1° , 2° , and 3° boxcar filter, respectively.

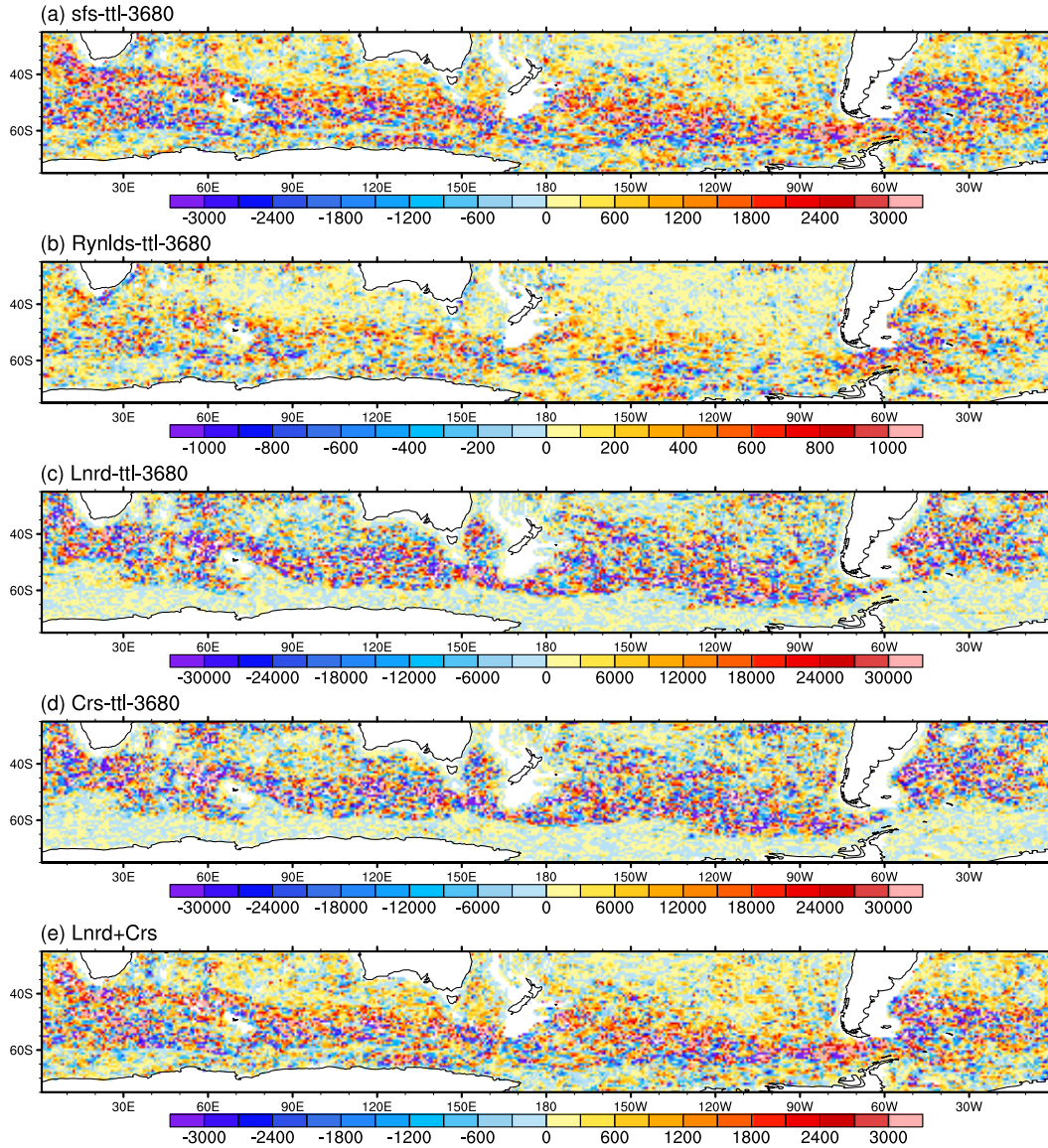


Figure C4. The eddy transport coefficient of (a) complete subfilter, (b) Reynolds term, (c) Leonard term, (d) Cross term and (e) Leonard plus Cross term, unit: m^2/s , on the topobaric surface of $36.8kg/m^3$, using 2° boxcar filter for SOSE

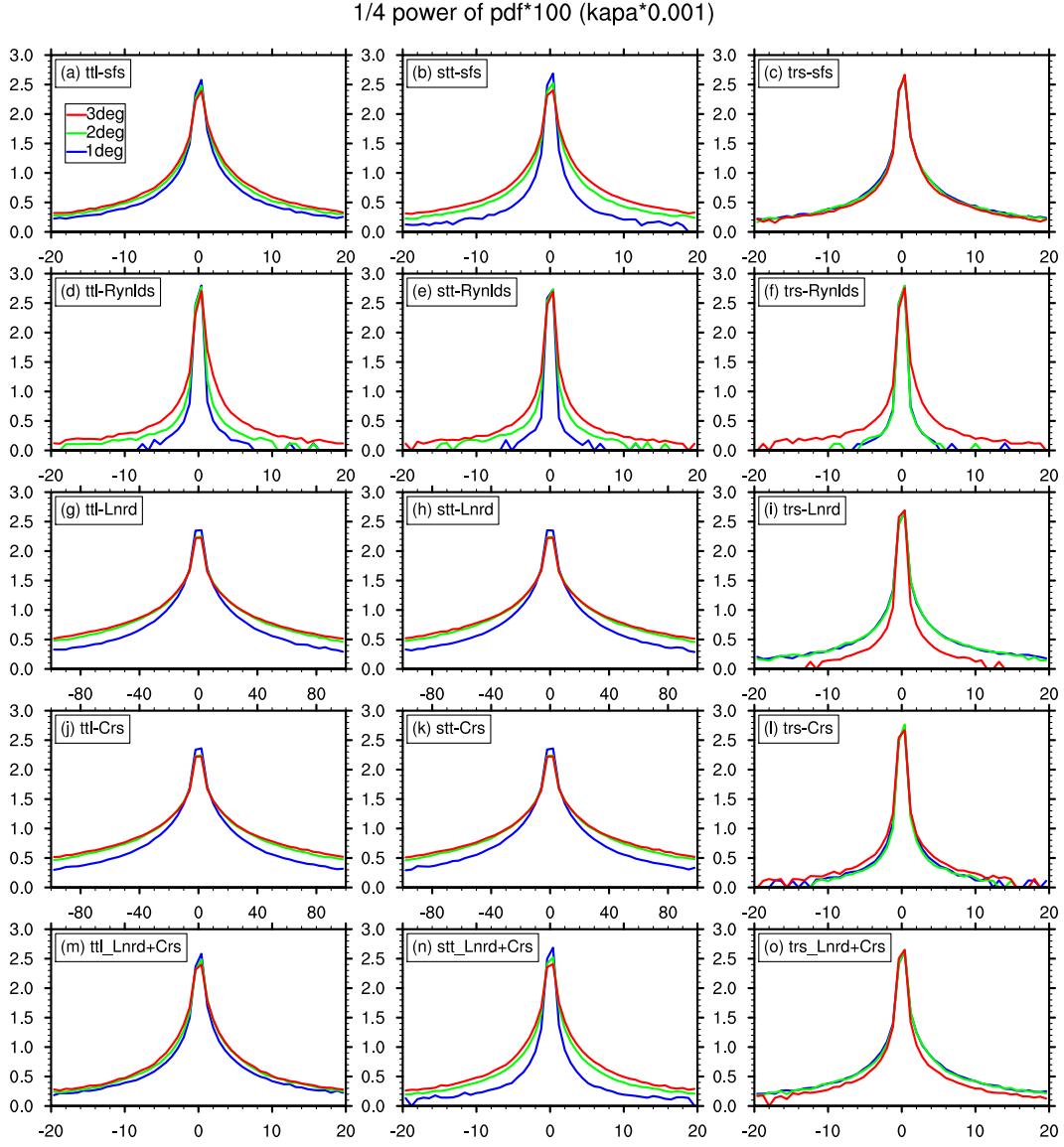


Figure C5. The same as Figure 3, but for the eddy transport coefficient $10^3 m^2/s$

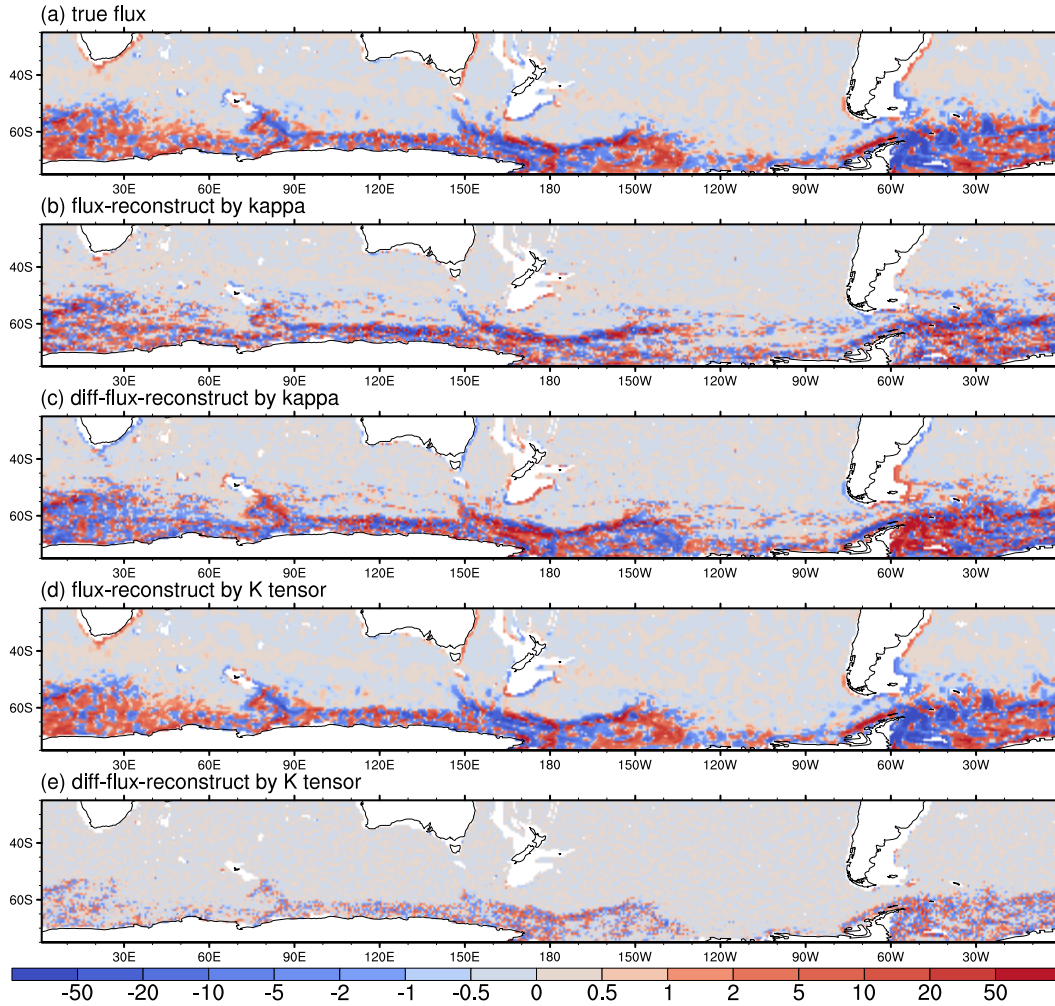


Figure C6. (a) The total meridional subfilter PV flux, (b) the flux reconstructed by the isotropic transport coefficient, (c) the difference between the isotropic reconstruction and true flux, (d) the flux reconstructed by the anisotropic transport tensor, and (e) the difference between the anisotropic reconstruction and true flux, on the topobaric surface of $36.8\text{kg}/\text{m}^3$, using 2° boxcar filter for SOSE

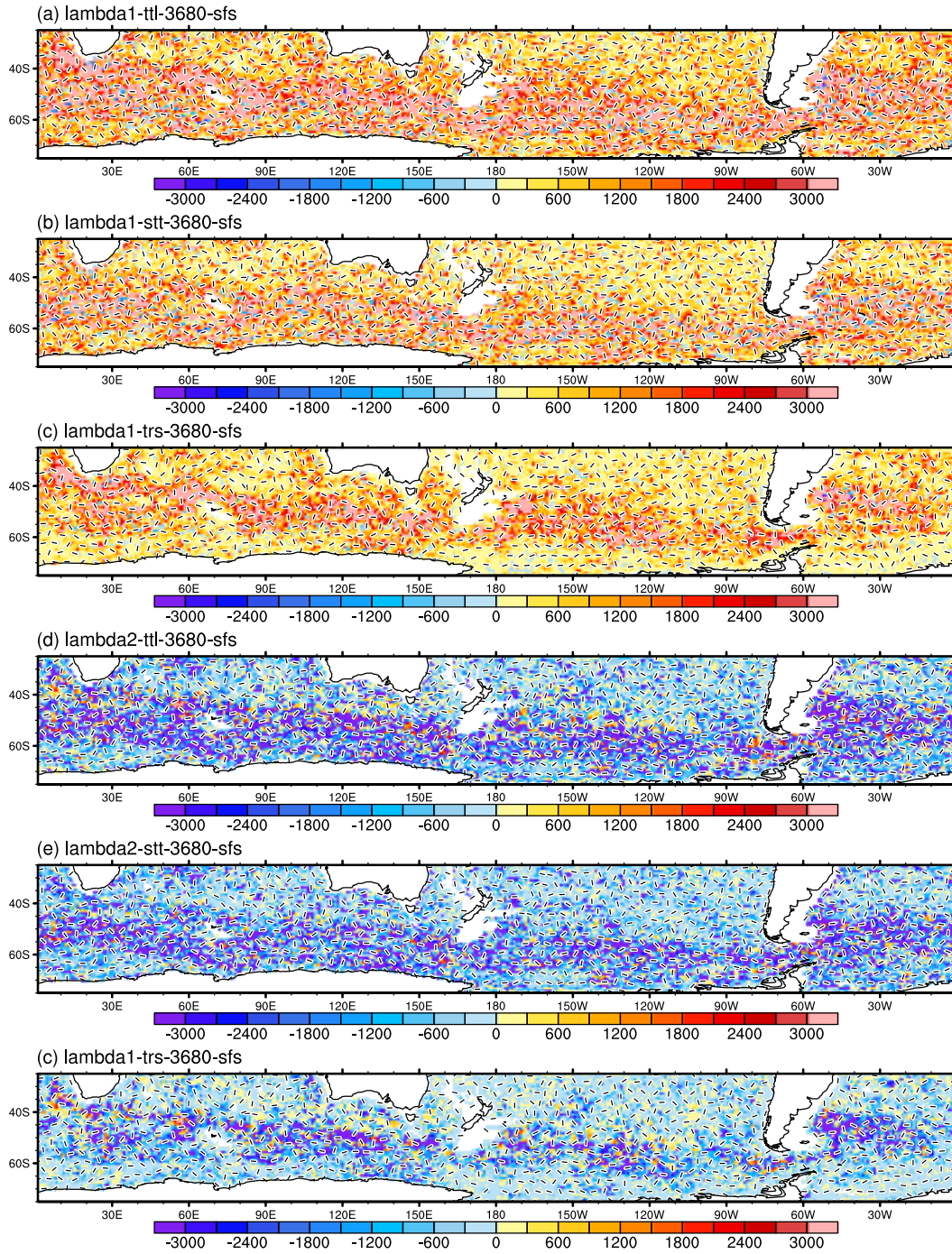


Figure C7. (a) (b) (c) is the total, stationary, and transient major transport eigenvalue respectively, (d) (e) (f) for the minor eigenvalue, on the topobaric surface of 36.8 kg/m^3 , using 2° boxcar filter for SOSE

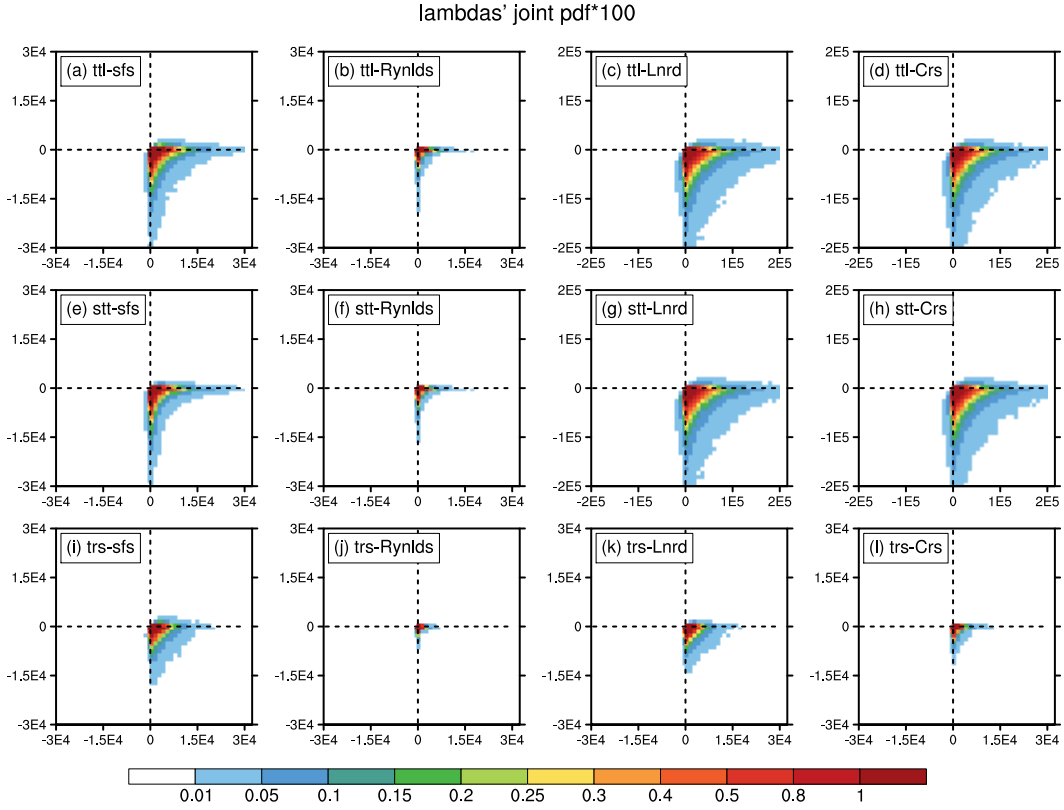


Figure C8. The joint PDF of the two eigenvalues of SOSE under 2° boxcar filter. The three rows from top to bottom are the total, stationary, and transient, respectively. The four columns from left to right are the results of complete subfilter, Reynolds term, Leonard term, and Cross term, respectively. The x- and y-coordinate represent the variation range of the major and minor eigenvalue, respectively (note that the coordinate range of different terms might be different). Values that are beyond the coordinate range or less than 10^{-4} are not shown. The bin interval is $1/25$ of the maximum coordinate value.

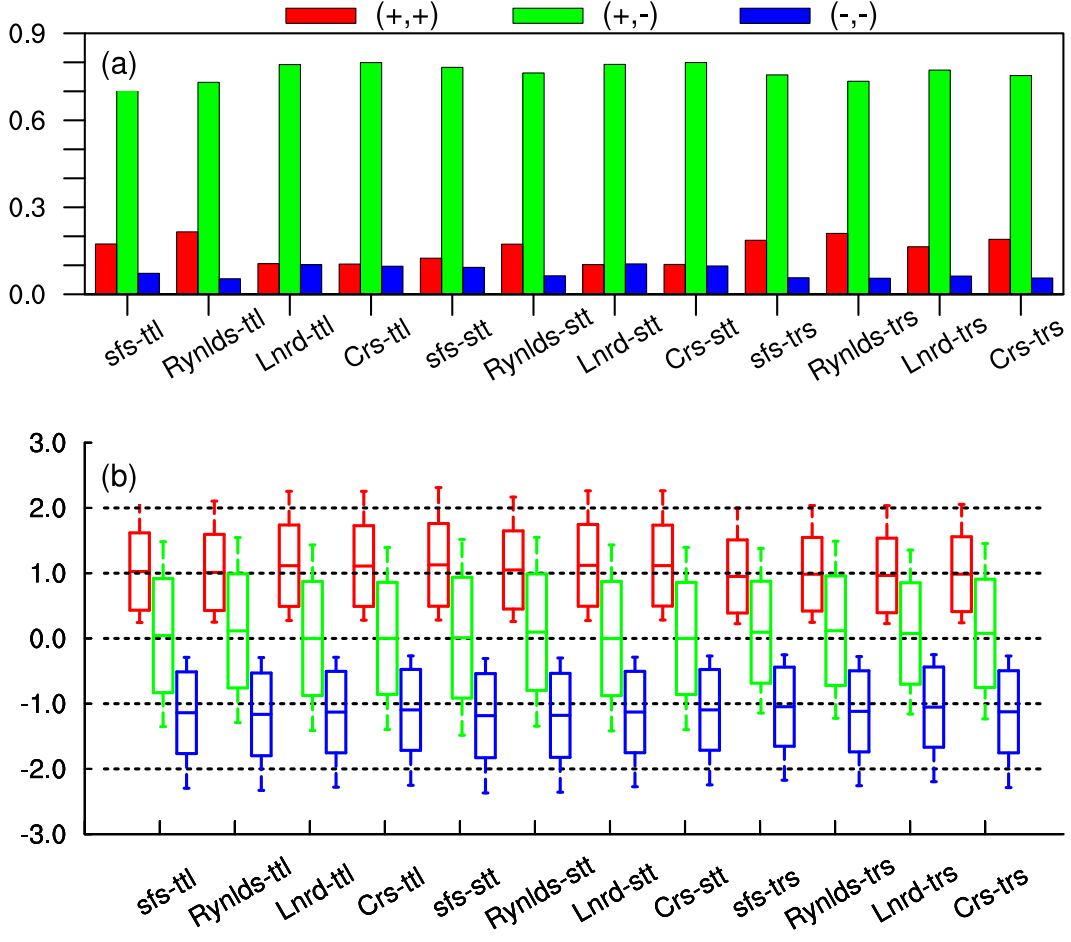


Figure C9. (a) The frequency of three eigenvalue combinations, (b) the degree of anisotropy, that is, the \log_{10} of the absolute value of the ratio of the major eigenvalue to the minor eigenvalue, on the topobaric surface of $36.8\text{kg}/\text{m}^3$, using 2° boxcar filter for SOSE. Red is (major+, minor+), green is (major+, minor-), and blue is (major-, minor-).

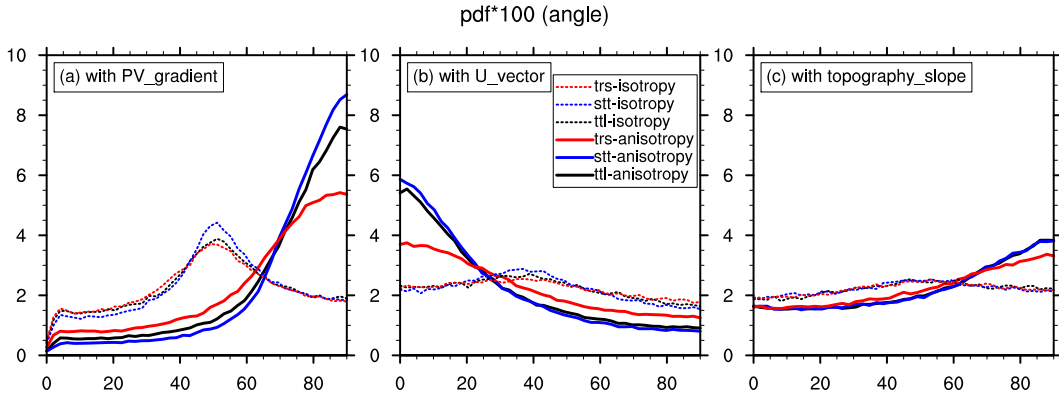


Figure C10. The PDF of the angle between the dominant eigenvector and the (a) topographic slope, (b) PV gradient and (c) velocity vector, on the topobaric surface of $36.8\text{kg}/\text{m}^3$, using 2° boxcar filter for SOSE. The solid line is for strong anisotropic region where $|\lambda_1/\lambda_2| > 5$ or $|\lambda_1/\lambda_2| < 1/5$, and the dotted line is for weak anisotropic region where $|\lambda_1/\lambda_2| < 1/2$ and $|\lambda_1/\lambda_2| > 1/2$. Black, blue, and red lines are for total, stationary, and transient parts, respectively. The topographic slope, PV gradient and velocity vector have also been 2° boxcar filtered

S1

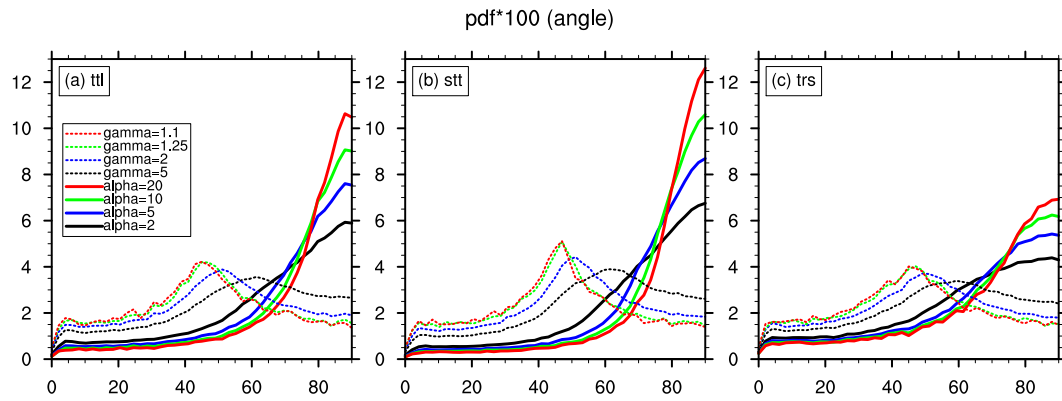


Figure C11. The PDF of the angle between the (a) total, (b) stationary, and (c) transient dominant eigenvector and the large-scale PV gradient on the topobaric surface of 36.8 kg/m^3 , using 2° boxcar filter for SOSE. The solid line is for strong anisotropic region with $\alpha = 2, 5, 10, 20$, and the dotted line is for weak anisotropic region with $\gamma = 1.1, 1.25, 2, 5$.

Supporting Information for ”A multifaceted isoneutral eddy transport diagnostic framework and its application in the Southern Ocean”

Jingwei Xie^{1,2}, Hailong Liu^{1,2,3} *, and Pengfei Lin^{1,2}

¹LASG, Institute of Atmospheric Physics, Chinese Academy of Sciences, Beijing 100029, China

²College of Earth and Planetary Sciences, University of Chinese Academy of Sciences, Beijing 100049, China

³Center for Ocean Mega-Science, Chinese Academy of Sciences, Qingdao 266071, China

Contents of this file

Figures S1 to S8

Introduction

The supporting information contains eleven additional figures (Figure S1 to S8) to support discussions in the main text.

*

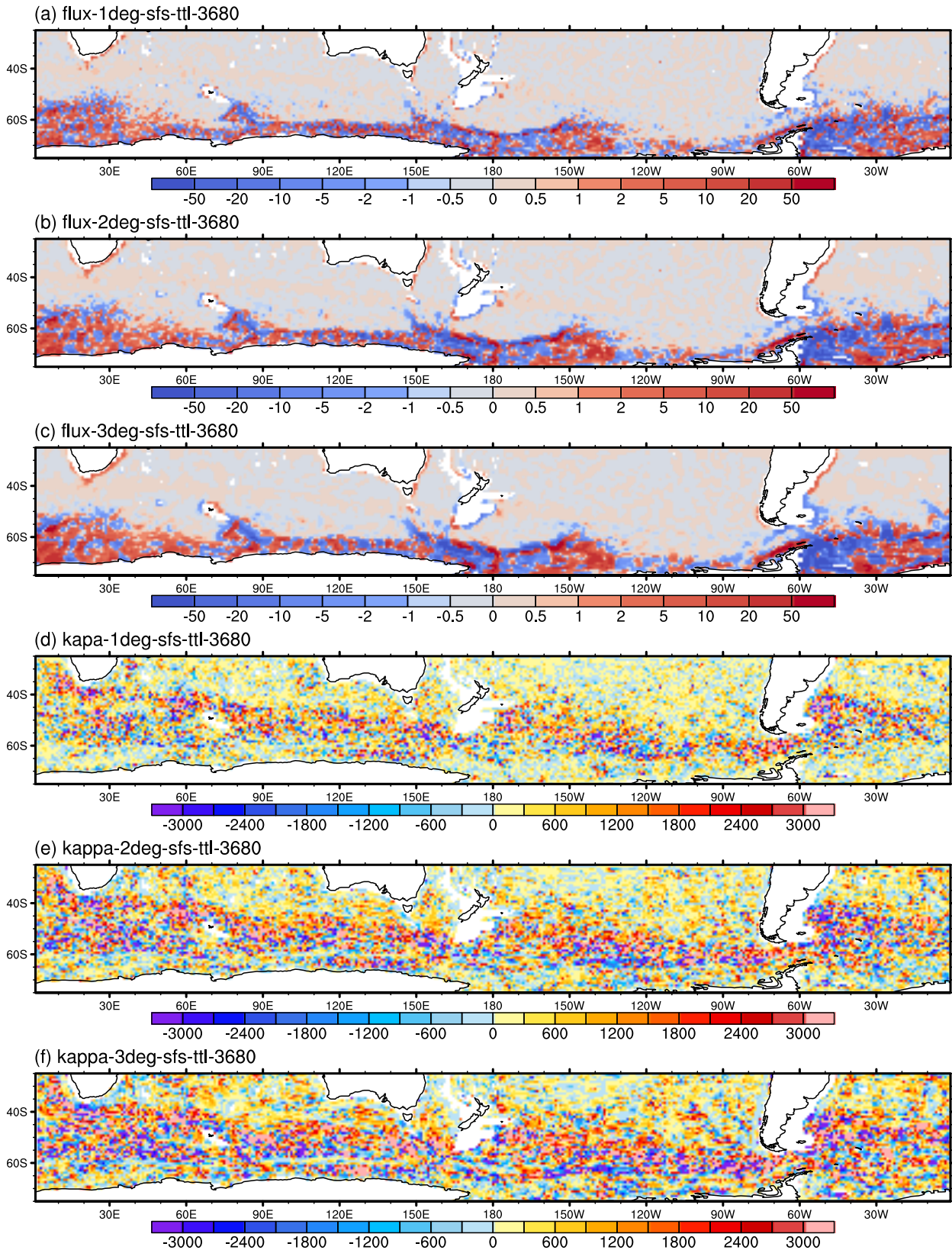


Figure S1. (a) (b) (c) is the total meridional subfilter PV flux with boxcar filters of 1°, 2° and 3° respectively, and (d) (e) (f) is the total subfilter transport coefficient, on the topobaric surface of 36.8 kg/m^3 for SOSE

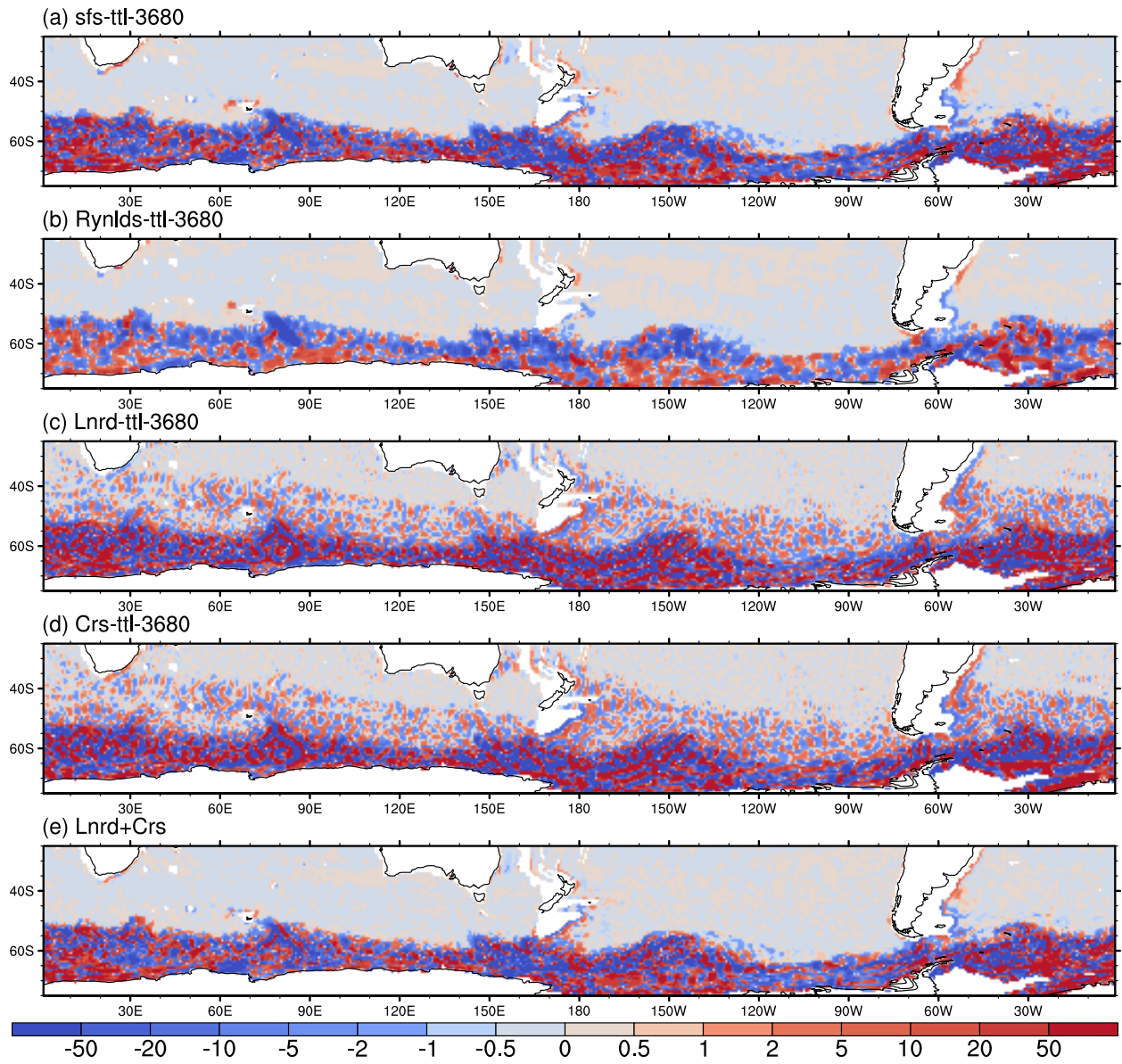


Figure S2. The same as figure 2, but on the σ_2 surface of $36.8\text{kg}/\text{m}^3$ for LICOM

June 3, 2022, 4:43pm

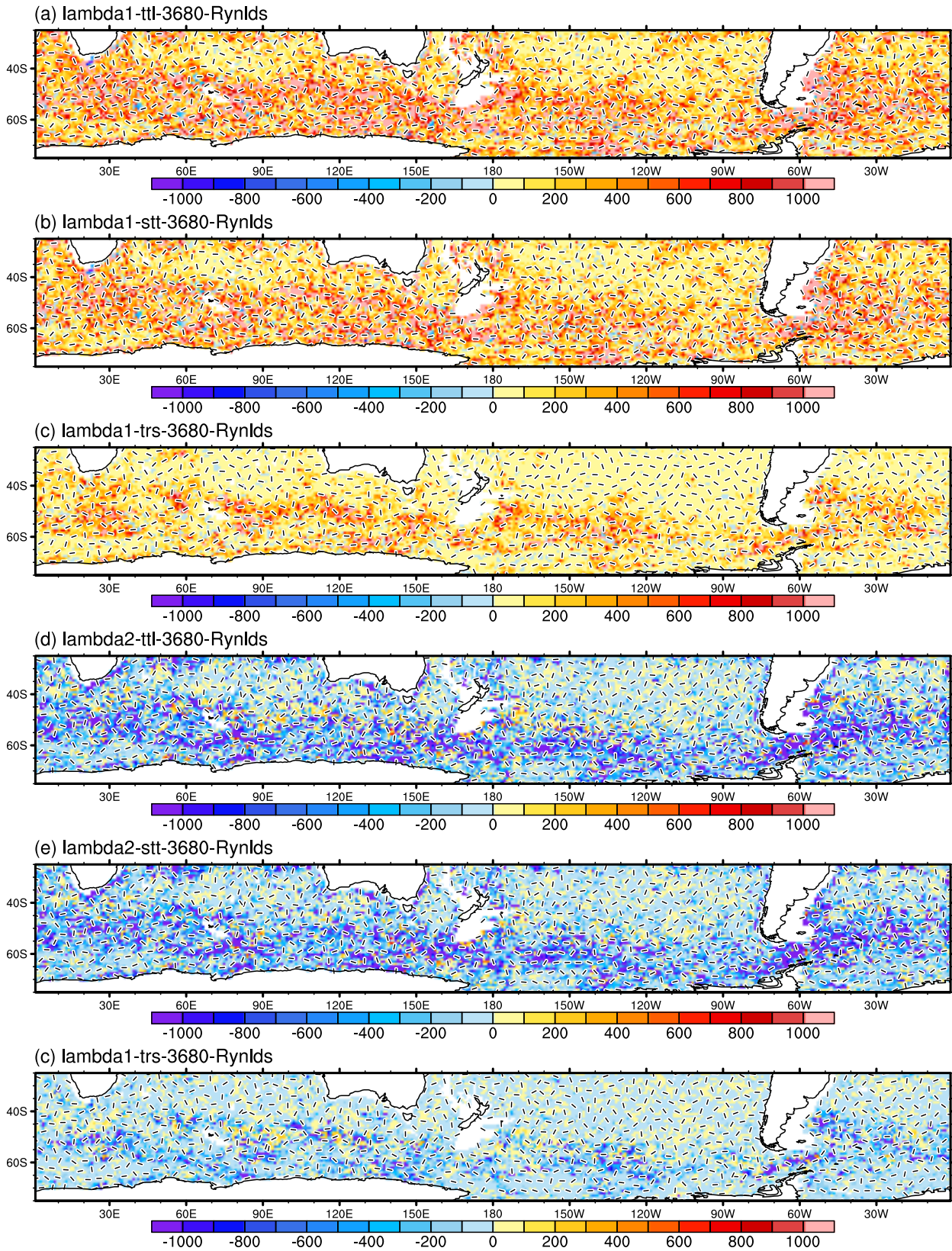


Figure S3. The same as Figure 7, but for the Reynolds term

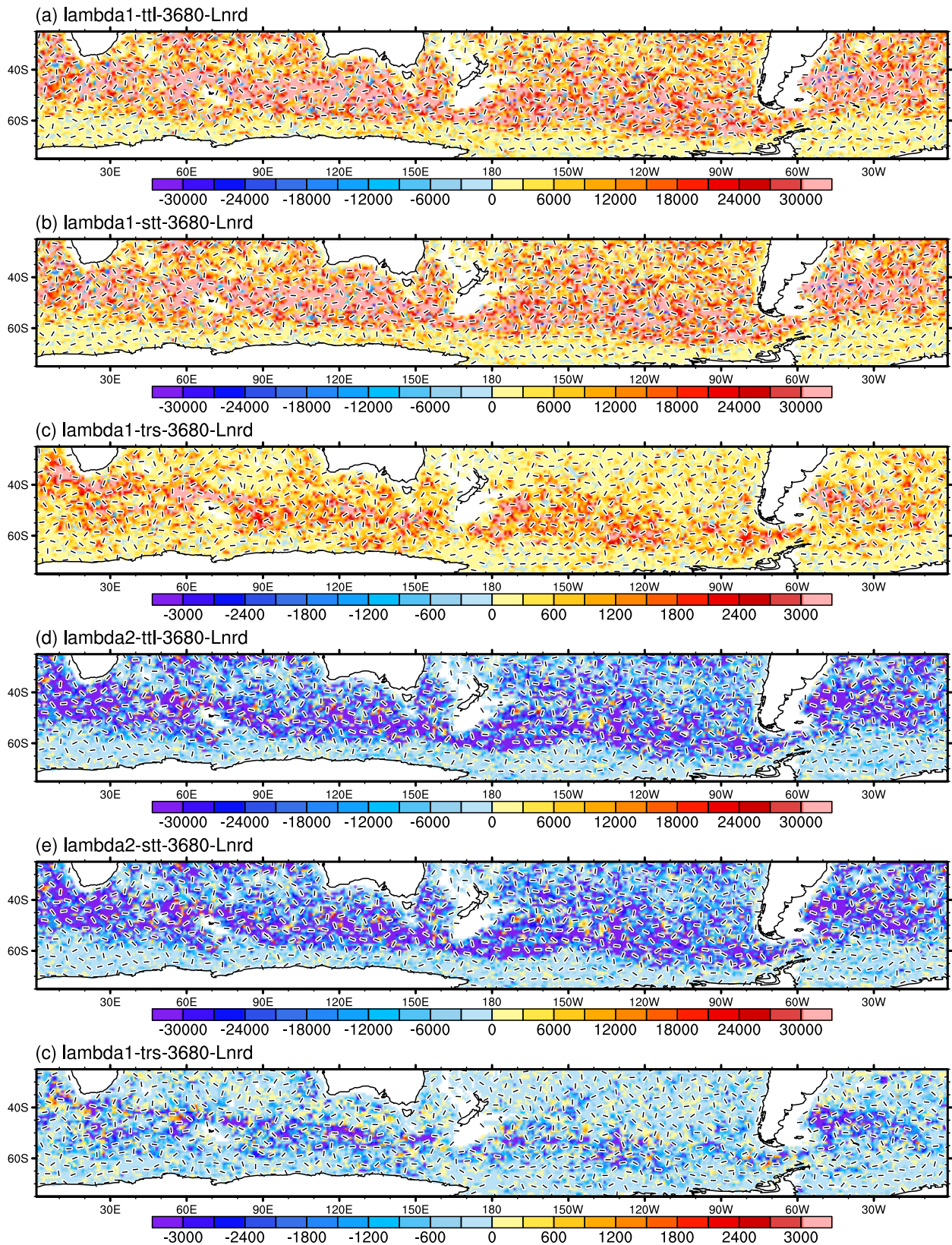


Figure S4. The same as Figure 7, but for the Leonard term

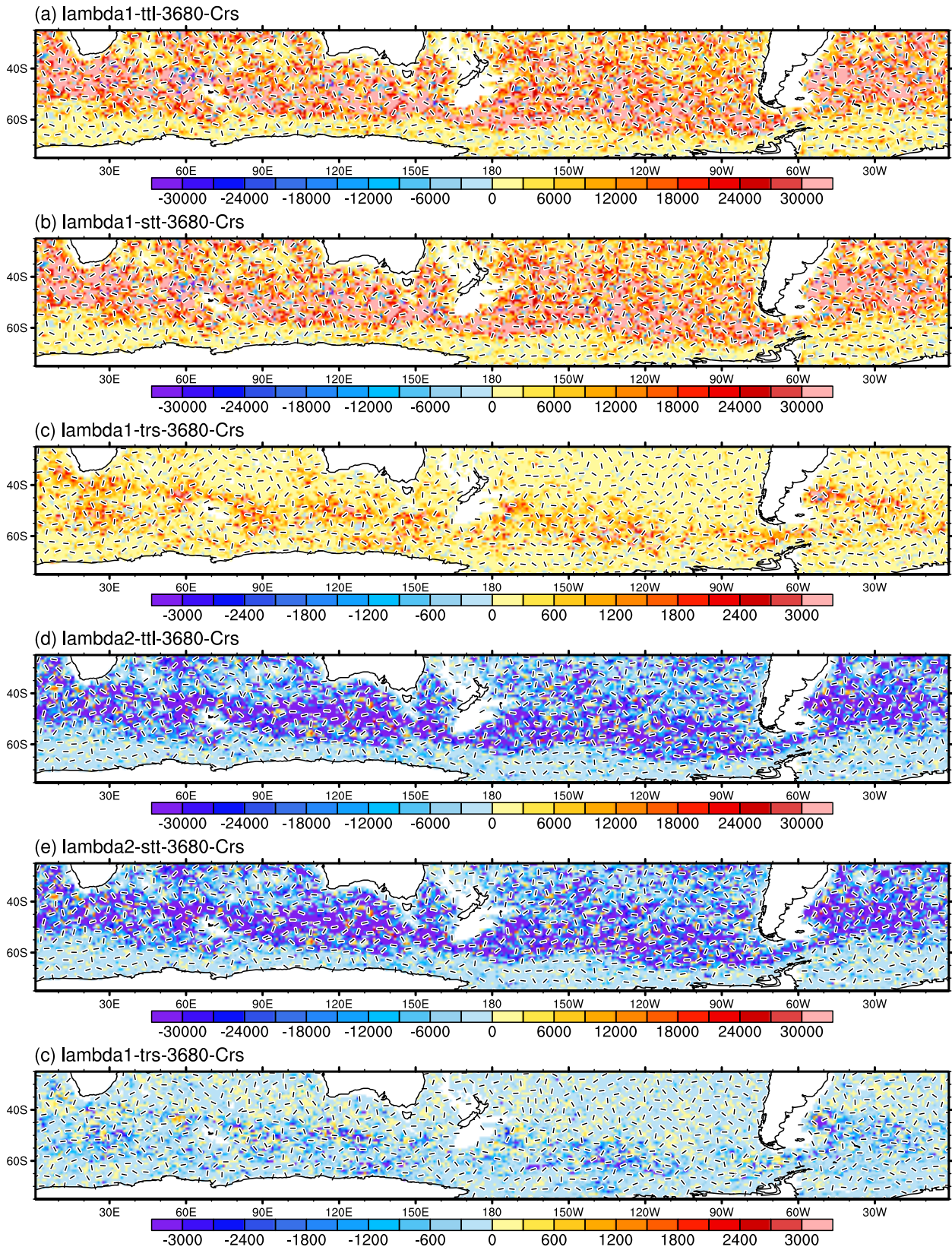


Figure S5. The same as Figure 7, but for the Cross term

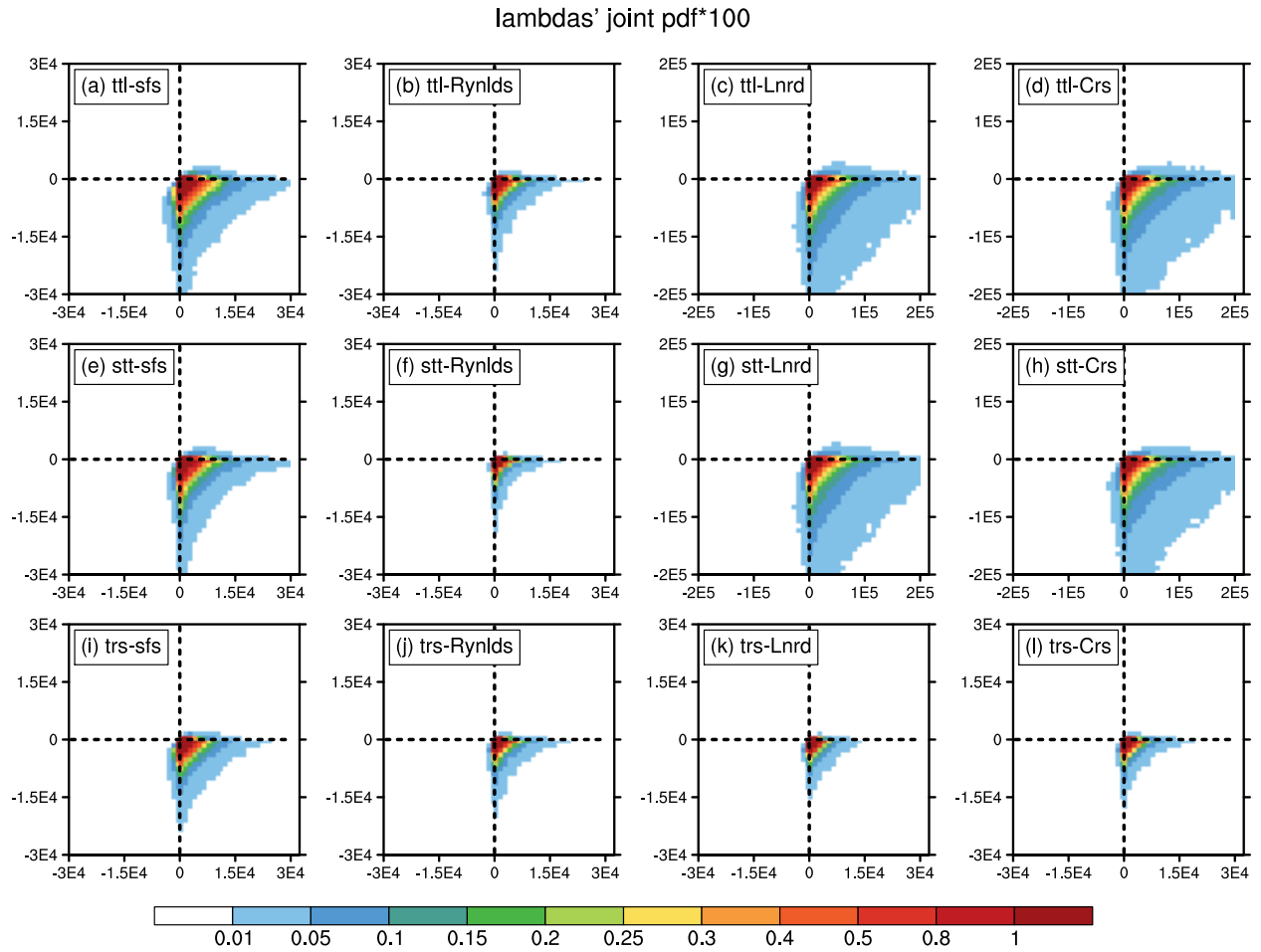


Figure S6. The same as Figure 8, but for LICOM.

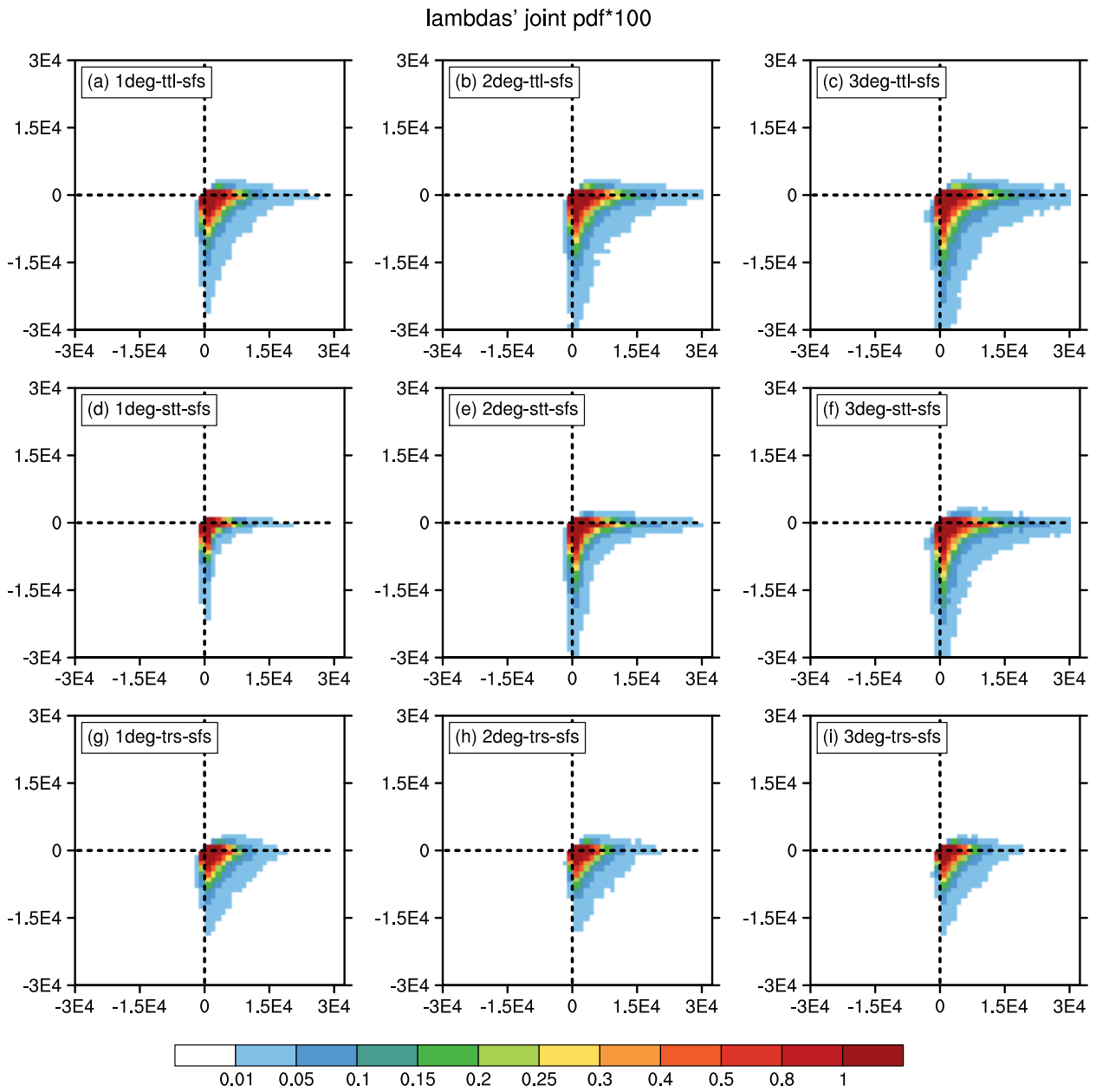


Figure S7. The joint PDF of the two eigenvalues of SOSE under different boxcar filters. The three rows from top to bottom are the total, stationary, and transient, respectively. The three columns from left to right are for 1° , 2° , and 3° , respectively. Other settings are the same as in Figure 8.

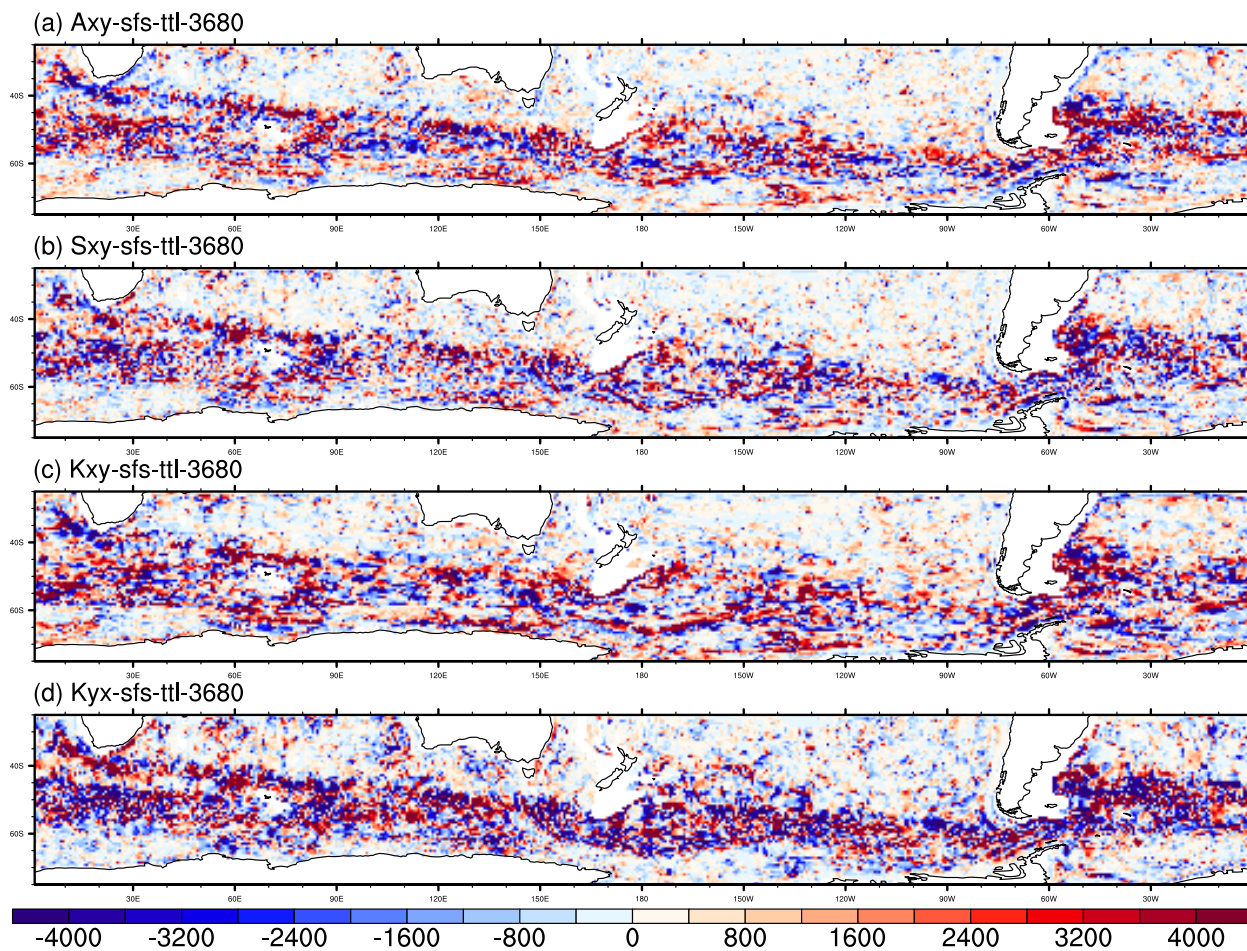


Figure S8. (a) The off-diagonal element A_{xy} of the antisymmetric part, (b) the off-diagonal element S_{xy} of the symmetric part, and (c)(d) the off-diagonal element K_{xy} and K_{yx} of the total subfilter transport tensor on the topobaric surface of $36.8\text{kg}/\text{m}^3$ for SOSE